BRNO UNIVERSITY OF TECHNOLOGY
VYSOKÉ UČENÍ TECHNICKÉ V BRNĚ

FACULTY OF MECHANICAL ENGINEERING
FAKULTA STROJNÍHO INŽENÝRSTVÍ

INSTITUTE OF PHYSICAL ENGINEERING
ÚSTAV FYZIKÁLNÍHO INŽENÝRSTVÍ

IN-SITU ELECTRON MICROSCOPY
IN-SITU ELEKTRONOVÁ MIKROSKOPIE

MASTER'S THESIS
DIPLOMOVÁ PRÁCE

AUTHOR — **Bc. Kristýna Bukvišová**
AUTOR PRÁCE

SUPERVISOR — **doc. Ing. Miroslav Kolíbal, Ph.D.**
VEDOUCÍ PRÁCE

BRNO 2019

BRNO UNIVERSITY OF TECHNOLOGY
FACULTY OF MECHANICAL ENGINEERING

Specification Master's Thesis

Department:	Institute of Physical Engineering
Student:	**Bc. Kristýna Bukvišová**
Study programme:	Applied Sciences in Engineering
Study field:	Physical Engineering and Nanotechnology
Supervisor:	**doc. Ing. Miroslav Kolíbal, Ph.D.**
Academic year:	2018/19

Pursuant to Act no. 111/1998 concerning universities and the BUT study and examination rules, you have been assigned the following topic by the institute director Master's Thesis:

In–situ electron microscopy

Concise characteristic of the task:

Electron microscopy is a widely used technique for complex analysis of nanomaterials. Quite recently, the interest of the community turned towards real–time observation of chemical reactions and physical processes. Such applications require new methodology, and are also demanding on innovation of microscope hardware. Student will focus on applications relevant for the supervisor's research group and her task will be to conduct the proposed experiments in an electron microscope.

Goals Master's Thesis:

1. Get trained to the available experimental apparatus.
2. Propose and conduct an experiment focused on observation of nanostructure growth (e.g. oxidation of WS2 nanotubes) and oxidation–reduction reactions within an SEM.
3. Analyze the results and perform additional characterization by relevant techniques. Study the beam effect (electrons, ions) on the proposed mechanism.

Recommended bibliography:

TAHERI, M. L., STACH, E. A., ARSLAN, I. et al. Current status and future directions for in situ transmission electron microscopy. Ultramicroscopy. 2016, 170, 86-95.

ZHENG, H., MENG, Y. S., ZHU, Y. Frontiers of in situ electron microscopy. MRS Bulletin. 2015, 40(01), 12-18.

Deadline for submission Master's Thesis is given by the Schedule of the Academic year 2018/19

In Brno,

L. S.

prof. RNDr. Tomáš Šikola, CSc. Director of the Institute	doc. Ing. Jaroslav Katolický, Ph.D. FME dean

Abstrakt
Cílem diplomové práce je popsat oxidaci nanotrubic sulfidu wolframičitého za zvýšených teplot v přítomnosti vodní páry. Na jejich povrchu se nejprve vytvoří nanočástice oxidu wolframu, ze kterých potom vyrůstají nanodráty. Na základě in-situ experimentů v rastrovacím elektronovém mikroskopu je navržen mechanismus reakce a ten je zjednodušeně popsán analyticky. Ukazuje se, že elektronový svazek má zásadní vliv na reakci.

Summary
The aim of this thesis is to describe oxidation of tungsten disulfide nanotubes at elevated temperatures in water vapour. On their surface, tungsten oxide nanoparticles are formed from which nanowires can emerge. Based on in-situ experiments in a scanning electron microscope, a mechanism is proposed and described analytically. The electron beam is found to strongly enhance the reaction.

Klíčová slova
In-situ rastrovací elektronová mikroskopie, dichalkogenidy přechodných kovů, nanodráty oxidů wolframu, růst nanodrátů

Keywords
In-situ scanning electron microscopy, transition metal dichalcogenides, tungsten oxide nanowires, nanowires' growth

BUKVIŠOVÁ, K. *In-situ Electron Microscopy.* Brno: Brno University of Technology, Faculty of Mechanical Engineering, 2019. 54 p. Supervisor doc. Ing. Miroslav Kolíbal, Ph.D.

I declare that I have written this thesis on my own, under the supervision of my diploma thesis supervisor. I have used no other resources, except those cited and mentioned in the references.

Bc. Kristýna Bukvišová

I wish to express my gratitude to my supervisor, doc. Ing. Miroslav Kolíbal, Ph.D., for his valuable guidance, comments and ideas. I owe my thanks to Mgr. Libor Novák, Ph.D. for the assistance with experiments in the SEM reactor, doc. Ing. Radek Kalousek for the consultation of the analytical description of growth rates and Ing. Lukáš Kachtík and Ing. Michal Horák for the help with TEM imaging of the grown nanowires and nanotubes. Last but not least, I am grateful to my family and friends who supported me during the studies.

Part of this work was carried out with the support of CEITEC Nano Research Infrastructure (ID LM2015041, MEYS CR, 2016–2019), CEITEC Brno University of Technology. I was supported by Thermo Fisher Scientific student scholarship.

Bc. Kristýna Bukvišová

Contents

1 Introduction **8**

2 Theoretical Basis **9**
2.1 In-situ Electron Microscopy 9
2.2 Material Stability under Electron Beam Irradiation 11
2.3 Tungsten Disulfide 13
2.4 Tungsten Oxides 16
2.5 Analytical Description of Vapour–Solid Growth Mechanism 20

3 Methods **24**
3.1 Instrumentation 24
3.2 Kinetics of Tungsten Oxide Growth 25
3.3 Determination of the Extent of Oxidation in WS_2 Nanotubes 26

4 Results **28**
4.1 General Information about the Process of WS_2 Oxidation 28
4.2 Measured Elongation of Nanowires 36
4.3 Growth Rates for Various Experimental Conditions 39
4.3.1 Influence of the Electron Beam 39
4.3.2 Influence of Temperature 42
4.3.3 Influence of Water Vapour Pressure 44
4.4 Cross-Sections of Nanotubes 44

5 Conclusions **48**

Bibliography **50**

1. Introduction

Exposing tungsten disulfide nanotubes to water vapour at elevated temperatures results in growth of substoichiometric tungsten oxide wires. The main objective of this work is to study these changes in real time, explain their mechanism and describe how various experimental conditions, including irradiation by an electron beam, influence the reaction products and kinetics.

During the development of synthesis strategies of metal oxides, their nanoscale modifications were obtained. Their properties differ from the bulk due to their geometry and nanoscale confinement. Tungsten oxides are prospective for use in gas sensing, field emission or electrical devices and their surface is known to be able to catalyse hydrogen evolution reaction. There have been attempts to control the growth of WO_x nanowires and in order to achieve that, understanding the reaction mechanism is crucial.

In the first part of this thesis (chapter 2), an introduction to in-situ electron microscopy and electron-beam-induced damage are presented, followed by a brief overview of fundamental properties of tungsten disulfide nanotubes and previous experiments providing tungsten oxides in various phases.

Different stages of WS_2 oxidation in water vapour are described in section 4.1. First, the nanotube is decorated with tungsten oxide nanoparticles which tend to be organized in lines which show chirality of nanotubes and edges of incomplete outer WS_2 sheets. Then, not only from the nanoparticles, tungsten oxide nanowires emerge. Their elongation can be observed directly in standard high-vacuum SEM with a special reactor holder (section 3.1). Apart from nanotubes, oxidation of platelets was tested as well.

Based on the measurements and observations, a model for the growth of nanowires is formulated and described analytically with many simplifications in section 2.5. The model is later used for fitting experimental data in section 4.2. The influence of water vapour pressure, reaction temperature and electron beam irradiation is studied in chapter 4. In order to see possible morphological changes of nanotubes when they undergo oxidation, their cross sectioning was done. The cross sections showed that they can have elliptical shape and that strain effects could influence the reaction.

2. Theoretical Basis

2.1. In-situ Electron Microscopy

Electron microscopy has become one of the most important and widely used techniques for the analysis from macro- to atomic scale. It is conventionally performed ex-situ, i.e. before and after the sample undergoes a process under study. The rise of in-situ electron microscopy has been initiated in the 1960s when scientists desired to directly observe phase transformations and failure phenomena. Environmental microscopes have been first developed to aid the study of biological samples and to help to mitigate the formation of hydrocarbon contamination [1]. One of the pioneering works in the field of in-situ electron microscopy [2], done in collaboration with JEOL and published in 1968, was a direct observation of growth of zinc oxide needles at elevated temperatures. Since the late 1990s, wide commercialisation of low-vacuum and environmental secondary electron microscopes (SEM) and transmission electron microscopes (TEM) has been achieved [3, 4].

During the past decade, obtaining high quality live data from SEM and TEM in order to study changes of structure, chemistry, magnetic and other properties, has been enabled with progressing technologies, e.g. aberration correctors, microelectromechanical systems (MEMS) and integration of optical systems into the imaging system [5]. Aperture-limited gas flow within a windowed cell enables a study of solid–liquid and solid–gas reactions within TEM and SEM, such as synthesis of nanoparticles and nanowires, catalysis, or charge transfer within prospective battery materials. For liquids with high vapour pressure, sealed reactor cells such as graphene liquid cells separate the sample from vacuum environment and for example enable direct observation of nanoparticle formation with very low background signal [6]. Sometimes, a gas leak provides a way to introduce nanostructure growth on clean samples. In the environmental transmission electron microscopes (ETEM), the desired gases fill the whole sample volume and the column is protected from the high pressure by a system of pressure-limitung apertures. A compromise between resolution and objective polepiece gap must be made especially for uncorrected systems [5].

For some experiments, knowing the composition of the analysed specimen is desirable. Energy dispersive X-ray spectroscopy (EDS) is not very well suited since the detector can be damaged by the reactive gases and it gets swamped by thermal radiation when a heating stage is used. Electron energy loss spectroscopy (EELS) is much better for this purpose. It has another big advantage — it detects a presence of elements with high spatial resolution. Especially when nanostructures are grown, fine changes of composition need to be identified [7].

Even though the gap between the capabilities of SEM and TEM has been narrowing in the past years, most of the attention nowadays is focused on in-situ TEM due to its resolution. In SEM, a wider variety of experiments can be realized since the amount of spectrometers and other microscopic or mechanical systems which fit under the objective in the chamber is higher. One of the examples is in-situ SEM mechanical testing in material science [8]. It enables probing surface deformation behavior while various loading conditions such as tension, compression, cyclic fatigue and creep can be applied. Additionally, these experiments can be conducted under different temperatures and pressures. Combination of imaging with EDS as well as determination of crystallographic orienta-

tions with electron backscatter diffraction allows for a complex analysis of mechanical transformations [8]. Unlike in TEM, the specimen does not need to be transparent for electrons in SEM and, therefore, the preparation and dimensions of the analysed sample are not limited. In-situ TEM is only well suited for experiments where the dynamics on atomic scale are slow or comparable to the temporal resolution of the system.

The signal to noise ratio (SNR) is influenced by the experimental conditions (heated stage and ambient gas) and in SEM, secondary electron images suffer problems with noise due to thermionic emission especially for temperatures higher than 900 °C [4]. SNR is influenced by the pixel aquisition time as well. In SEM, the frame rate usually ranges between 30 frames/s to 1 frame/min [4]. A compromise between spatial and temporal resolution must be made, which is especially important for gas-solid processes such as oxidation or vapour deposition [9]. The reactions are made slower in ETEM by lowering the pressure of the gas phase. In ESEM, large-scale analysis is accessible and higher pressures of the reactive species are available. SE contrast is very sensitive to surface alterations so, for example, it is possible to study diffusion fronts of molecules on the surface [9]. The possibility to prepare a sample utilizing focused ion beam and nanomanipulators and directly conduct in-situ SEM experiments without exposing the sample to atmospheric conditions during its transfer must be mentioned here as well.

One of the issues which must be tackled is the influence of the electron beam itself. Some materials are damaged upon the interaction with the electron beam (knock-on, radiolysis) and contamination is quite often present. Especially if chemical reactions are studied, ionization and knock-on damage must be considered. Of course, vacuum conditions, temperature of the sample, e-beam energy, current and dose as well as the properties and geometry of the studied specimen can play a major role. There is a great difference between the beam effects in TEM and SEM. In SEM, the dose rate is decreased significantly and beam effects are, in most cases, less pronounced than in TEM [9]. Sometimes, it is possible to determine how the reaction proceeds without the interference of the beam [3]. Using a large amount of data for different doses, it is possible to extrapolate the behaviour for no irradiation. In section 2.2, the principles of electron beam damage under different experimental conditions will be discussed.

Apart from the principal concerns, imaging with a heated specimen stage has to deal with thermal drift. Drift correctors eliminate this problem and especially for TEM, these correctors are often incorporated within the camera system. Determining the actual temperature at the point of observation is a long discussed issue. The situation is easier if no ambient gas surrounds the sample. In such case, only thermal contacts and conductivities play roles. If a gas is introduced, temperature gradients are strongly influenced by the gas flow. There have been multiple approaches how to determine the local temperature with high precision. One of them used electron energy loss spectroscopy of the gas phase determining local gas concentration and its correlation with ideal gas law [10].

The last but not the least is the issue of the subsequent data analysis — if fast changes are to be studied, a high sampling rate is necessary and the resulting amount of data can be significant. New approaches to data compression automatic analysis are a necessity for the future efficient utilization of in-situ observation.

2.2. Material Stability under Electron Beam Irradiation

Beam damage is a result of interactions of electrons with atoms or atomic electrons. When an energetic electron collides and transfers momentum to a bound atom, it can result in an atomic displacement. A Frenkel pair which consists of a vacancy and an interstitial atom is created. This is referred to as knock-on damage. The energy transfer can be derived from the laws of conservation energy and momentum. The energy ΔE acquired by the atom during the collision can be written as [11]

$$\Delta E = \frac{2E(E+2E_0)}{Mc^2} \cdot \sin^2\frac{\theta}{2} = T_m \cdot \sin^2\frac{\theta}{2}, \tag{2.1}$$

where E is the kinetic energy of the incident electron, $E_0 = m_0c^2$, m_0 is the rest mass of the electron, c the speed of light, M the mass of the target atom and θ is the scattering angle of the primary electron after the collision. T_m is the maximal transferred energy for the scattering angle 180°. Knock-on damage occurs when the transferred energy exceeds the threshold energy for atomic displacement E_d which is the property of the specimen (bond strength and type, atomic weight, crystal lattice). The lighter the elements, the higher ΔE. If a binary compound is studied, the lighter element will be sputtered preferentially. That results in nonstoichiometry within the irradiated area [11, 12].

The knock-on damage cross section σ_K expresses the probability that an energetic electron undergoes the scattering event and can be written (in barns, 1 barn=100 fm^2) as [11]

$$\sigma_K = 6.547 \cdot 10^4 \cdot \frac{1}{E^2}\left(\frac{E+E_0}{E+2E_0}\right)^2 \cdot \frac{Z^2\,(T_m - E_d)}{(\alpha+1)(\alpha T_m + E_d)}, \tag{2.2}$$

where α is the screening factor, E is the energy of the primary electron in keV, E_d is the displacement energy in eV, T_m is the maximal transferred energy calculated from equation 2.1 in eV. Using the Wentzel atomic model for the screening [13], α can be written as

$$\alpha = 3.43 \cdot 10^{-3}\frac{Z^{2/3}}{E(1+E/1022)},$$

where E is the primary electron energy in keV as well. When these equations are put together and plotted, we see that the only variables influencing the knock-on damage are M, Z, E_d and E. The cross sections calculated from the equation 2.2 are plotted for illustration in Figures 2.1 and 2.2.

Knock-on damage is mainly a problem in (S)TEM due to the energies involved. However, questions arise — what role does the temperature of the sample play and is it possible to induce knock-on damage in SEM as well? There are a few studies [14, 15, 16] on temperature-dependent beam damage and the main conclusion is that the dependence of knock-on damage is not strong (almost no difference in the threshold accelerating voltage was calculated for 0 K and 300 K in reference [14]), however it can play role in explaining sputtering below theoreticaly calculated threshold energies. It is necessary to note that already zero-point phonon modes are a sufficient explanation for the increased sputter rate compared to the static lattice [14]. The energies characteristic for lattice vibrations are negligible compared to the energies needed for the displacement of atoms but the movement of the atom significantly changes momentum transfer. Cooling TEM specimens

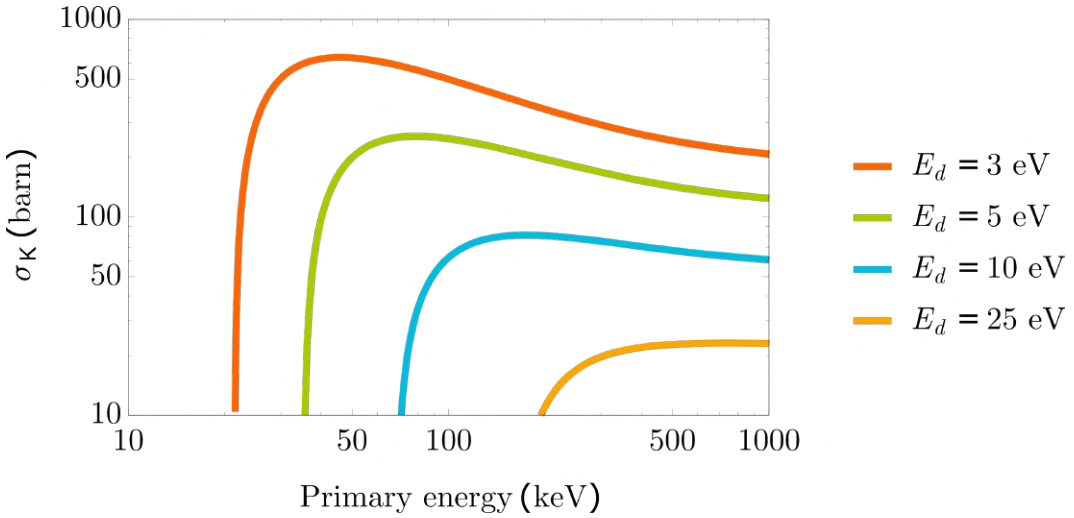

Figure 2.1: Calculated cross sections for knock-on damage for oxygen. With higher displacement energies, the threshold primary beam energies shift to higher values.

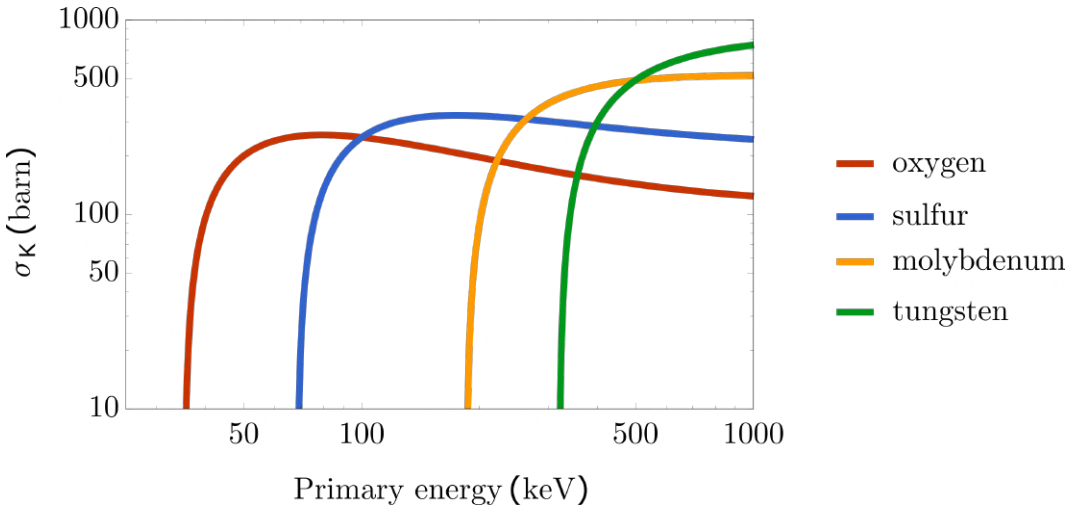

Figure 2.2: Calculated knock-on damage cross sections for multiple elements. The displacement energy is 5 eV in all cases. Higher atomic number of an element results in an increase of the lowest primary beam energy which causes knock-on damage. That is in correspondence with the increased ΔE for lighter elements.

is advantageous but mainly because the radiolytic processes are reduced, not knock-on damage [15]. In [16], beam-induced displacement of 2D TMDs was simulated using DFT calculations. The initial velocity of the target atom was calculated from the momentum transfer upon the electron impacting the atom and the system evolved in time. Thermal effects were taken into consideration but just as in [14], the difference between static (0 K) and vibrating lattice (300 K) did not give significantly different results. The main difference from dependence similar to Figs. 2.1 and 2.2, is a smooth onset of cross sections before the static threshold primary energy rather than a sharp onset at a specific energy. Edge S atoms had a lower displacement energy than those located far from the edge (for WS_2 ribbon, edge atoms had displacement energy of 4.2 eV compared to 7.0 eV for an inside atom).

If an electron interacts with an atomic electron in a nonelastic event and the localized excited state has a long enough lifetime (approximately ps), radiolytic beam damage can be caused. The situation is therefore different for conductors and insulators — in electronic conductors, the lifetime is in the order of fs but for insulators, the time can be much longer than ps [11]. Rather than an energy threshold, there is a minimal dose rate.

Radiolytic processes are caused by nonradiative relaxation of excitations. Breaking a chemical bond must be followed by an additional mechanism which displaces the atom such as thermal vibration and local Coulomb repulsion. It is usually the Arrhenius law that governs the rate of this type of damage [11]. Especially transition metal oxides are prone to be damaged by the electron beam in this way. The damage starts by O desorption from the surface and is often followed by a formation of a new phase inside the material due to diffusion of inner O atoms to the surface [11].

Another consequence of nonelastic collisions is beam induced heating. When an electron beam is confined within a small area, radiolytically enhanced diffusion and thermal diffusion can both take place [11].

The beam can introduce electric field (DIEF — damage due to induced electric fields) and therefore induce migration of ions in the material. The field is most prominent near the surfaces. For atoms with ionic bonds under the strong electric field, the bonded atoms can be even displaced if the work done by the field on the ion is larger than the activation energy for migration. The situation resembles to that of a capacitor charging since the process is collective [11].

2.3. Tungsten Disulfide

General Properties

So-called transition metal dichalcogenides (TMDs) are MX_2 compounds, where for example M = Mo, W, Ti or Nb and X = S or Se. In their 2D modifications, each trilayer sheet consists of bonded atomic layers organized hexagonally. The trilayers stack together because of weak van der Waals forces. The structure is similar to graphene but single hexagonal layer is replaced with a trilayer with different physical and chemical properties. A schematic of two trilayers bonded by van der Waals forces is in Fig. 2.3.

For smaller molecular sheets, the relative number of rim atoms with unsaturated bonds becomes significant. Because of these dangling bonds at the edges of sheets, closed structures are energetically favoured [18]. The sheets can be rolled in many directions, giving rise to nanotubes of different chirality. The discovery of inorganic nanotubes and fullerene-like structures based on TMDs in 1992 [19] gave rise to a great number of proposed and realized applications. TEM micrograph of WS_2 nanotube is in Fig. 2.3.

In bulk, the TMDs are semiconductors with indirect band gap, whereas in the sigle layer modification, they have direct band gap with energies corresponding to visible or near-IR light. Since they can be isolated into single or few-layer nanosheets and, unlike graphene, they have energy band gaps, their potential use in electronic devices is huge. For example, they could make up atomically thin transistors as well as optoelectronic and light emitting devices [20]. Incorporation of TMDs into 2D heterostructures has shown some potential in recent years.

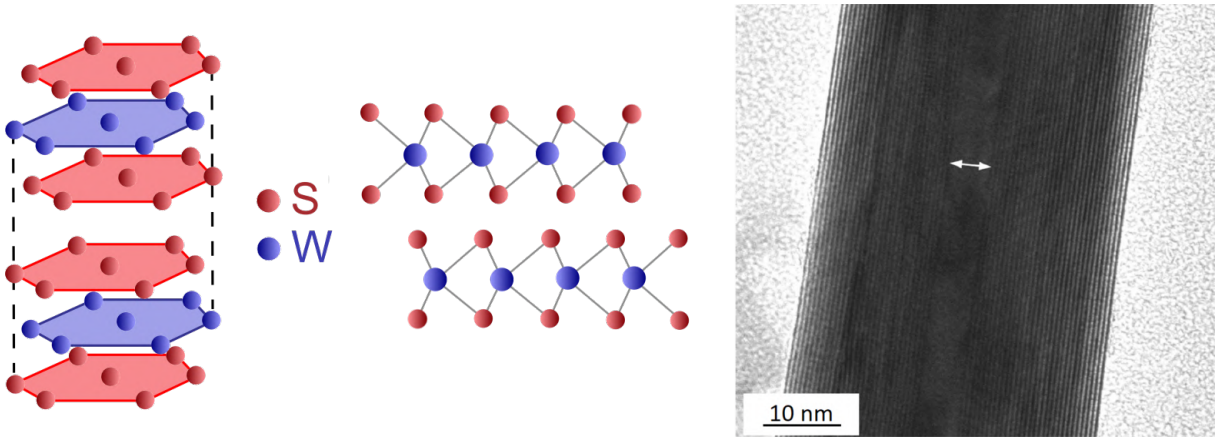

Figure 2.3: Left: In each sheet of WS_2, tungsten is sandwiched between two sulfur layers comprising of hexagons. Right: TEM micrograph of WS_2 nanotube. The white arrow shows the hollow core of the nanotube. TEM micrograph adapted from [17] and edited.

The energy gap of fullerene-like WS_2 nanoparticles and nanotubes decreases with lower diameter of the nanoparticles, which is in a contrast to results in semiconductor quantum dots. This behavior is strain-governed and not determined by quantum effects [18]. Interestingly, their band gap varies with the number of molecular layers as well [21].

Flexibility under tensile and torsion forces and strength was demonstrated for WS_2 nanotubes and these mechanical properties make them suitable for reinforcing polymer matrices. For example, bulk TMDs are used as commercial solid-state lubricants. Fullerene-like nanoparticles have been shown to outperform the bulk material so to an extent, they have replaced the bulk material. Main mechanisms for reducing friction are rolling of the nanoparticles and their exfoliation and transfer of sheets onto the lubricated interfaces [18]. Their catalytic properties are interesting if compared to bulk as well. Alkali metal atoms can be intercalated within fullerene-like MoS_2 and WS_2 and their nanotubes at elevated temperatures [22, 23]. The weak van der Waals forces enable the introduction of foreign compounds between the layers. The intercalation causes a substantial increase in the inter-planar spacing. First, molecules or atoms are adsorbed on the surface and then slowly diffuse inwards. For nanotubes, nanocapilarity helps the incorporation as well.

Synthesis of Tungsten Disulfide Nanotubes

Fullerene-like WS_2 nanoparticles and nanotubes were first synthesised by sulfidization of thin W films on top of quartz in H_2S atmosphere at elevated temperatures and shown to be stable [19].

Later, the conversion of tungsten trioxide nanoparticles into fullerene-like structures was realized. The sulfidization of oxide nanoparticles takes place at elevated temperatures, e.g. 700 °C. The process has two steps: firstly, the surface of the oxide is encapsulated by a single or double WS_2 layer within a few seconds which acts as a barrier against the fusion of the nanoparticles into a larger one. Secondly, a slow diffusion-governed process takes over and sulfur diffuses inwards and replaces oxygen in the core of the nanoparticle. Since the product has a higher density compared to the starting material, the resulting WS_2 particle has a hollow core [24].

One of the other approaches to obtaining the nanotubes, is to start from a precursor ammonium salt such as $(NH_4)_2WS_4$ and decomposing the formed trisulfide [25].

WS_2 nanotubes can be grown in larger amounts in two ways — spontaneous growth of oxide nanowhiskers from WO_{3-x} powder and their rapid sulfidization, which is driven by fast kinetics, and a slower conversion of tungsten oxide nanowhiskers through diffusion governed processes (similar to the preparation of nanoparticles in [24]). The latter is preferred since it allows better control over the reaction. Most of these approaches are based on higher temperature reactions of H_2 and H_2S with metal oxide nanowires ($W_{20}O_{58}$ or $W_{18}O_{49}$). The nanowires or nanowhiskers transform into nanotubes which reflect their diameter. A very important role in the reaction is played by a volatile hydrated suboxide phase. The remaining oxide in the core of the forming nanotube reacts with H_2S gas at the tip of the nanotube and contributes to its further elongation [17].

Oxidation of TMDs

There are some studies which deal with the effects of oxidative atmospheres on TMD based materials, especially their nanoscale modifications. Since O atoms have stronger electronegativity compared to other chalcogens, TMDs are prone to oxidation. TMD surface is more easily oxidized as the chalcogen atoms vary from S to Se to Te. It is logical to assume that this process starts at edges, grain boundaries or other defects where it is energetically most favourable. Since the grain boundaries are quite important for the properties of layered TMDs, easily accessible methods to visualize them are desirable. Selective oxidation can provide an easy way to make grain boundaries of 2D films visible. 20 min treatment of WS_2 at 380 °C in air results in oxide formation along the grain boudaries which become visible even in optical microscope [26]. Combining a presence of water vapour and UV irradiation works similarly to heating (Fig. 2.4) [27].

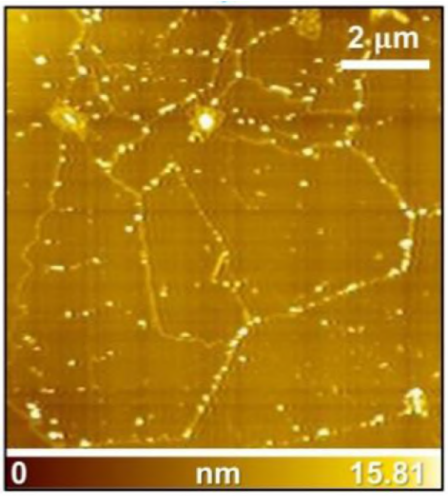

Figure 2.4: AFM image of an area of monolayer WSe_2 which was oxidized just by 6 min of UV treatment at elevated humidity [27].

2.4. Tungsten Oxides

Tungsten oxides exist in many forms, apart from stoichiometric WO_3 (α) and WO_2 (δ), many non-stoichiometric oxides were synthesized. However, only a few of them are stable — namely $W_{20}O_{58}$ (β) and $W_{18}O_{49}$ (γ). WO_3 and WO_2 particles are isotropic but the substoichiometric reduced WO_x are usually elongated because of their highly anisotropic lattice. When the powders undergo reduction, their morphology therefore changes significantly. The formation of WO_2, $W_{18}O_{49}$, $W_{20}O_{58}$, and WO_3 whiskers and wires has been often studied since the 1950s. It is suggested that when the conditions permit vapour transport, bundles of needle-like crystals are formed [28]. The crystal of stoichiometric WO_3 is comprised of a network of corner sharing WO_6 octahedra (Fig. 2.5 left.). When tungsten trioxide gets reduced, some of the octahedra share edges and the subsequent plane defects formed are called crystal shear planes (CS) (illustrated in Fig. 2.5). If they are ordered, a series of so-called Magneli phases are obtained. When more oxygen vacancies are formed, they are compensated by pentagonal columnar structures (PC) with hexagonal channels (HC) [28]. Schematic illustration of structure of $W_{18}O_{49}$ is in Fig. 2.6.

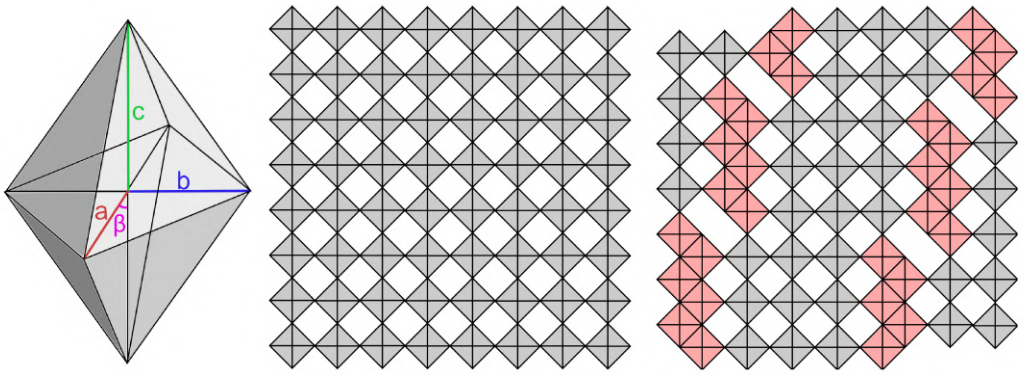

Figure 2.5: Left: The structure of WO_3 is monoclinic with lattice parameters $a = 0.7297\,\text{nm}$, $b = 0.7539\,\text{nm}$, $c = 0.7688\,\text{nm}$, $\beta = 90.91°\,\text{nm}$ [28] so the simplest visualisation is as an array of slightly distorted cubic structure. Middle: Ideal WO_3 structure comprised of corner sharing WO_6 octahedra. Right: An example of crystal shear planes when some of the octahedra share edges. The projections are along [0 1 0].

Heating (900 °C) WO_3 powder in H_2 atmosphere provides a way to easily observe some of these changes [29]. WO_3 is the most thermodynamically stable oxide. Upon reduction, WO_{3-x} crystals are formed and the final product is WO_2 or even W. The following reaction order is studied:

$$WO_3 \longrightarrow W_{20}O_{58} \longrightarrow W_{18}O_{49} \longrightarrow WO_2 \longrightarrow W.$$

In the first step of reduction, the powder (average particle size 7.5 µm in the study [29]) changes into plate-like whiskers, some of which form clusters. The lengths varied in the range of µm. The whiskers were converted to particles when WO_2 phase was formed. No significant change of morphology was observed when $W_{20}O_{58}$ was converted to $W_{18}O_{49}$. It was found that volatile tungsten compound $WOx \cdot nH_2O$ (where $2 < x < 3$) was probably formed when WO_3 was reduced and caused vapour-solid growth of whiskers. The most commonly observed stable phase of tungsten oxide whiskers and wires is γ-$W_{18}O_{49}$.

Monoclinic $W_{18}O_{49}$ nanowires often grow in [0 1 0] direction and the lattice parameters are: $a = 18.28\,\text{Å}$, $b = 3.775\,\text{Å}$, $c = 13.98\,\text{Å}$, $\beta = 115.20°$ [30].

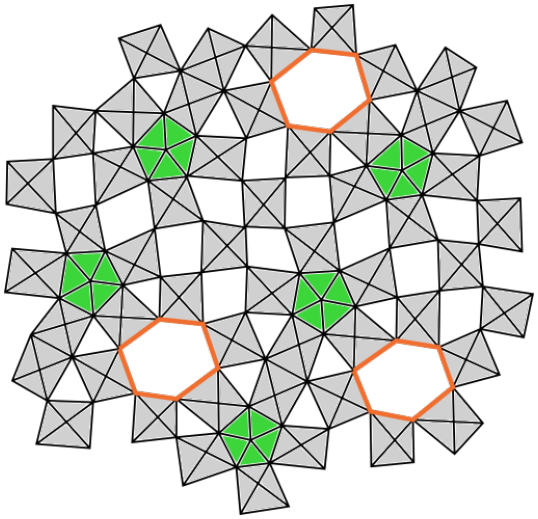

Figure 2.6: The structure of $W_{18}O_{49}$ — pentagonal columns are green, hexagonal channels are marked orange. PC comprises of five octahedra and a central pentagonal bipyramid. The ability of PC to fit into the original network is the reason for the existence of so many nonstoichiometric variants of tungsten oxide. The projection is along [0 1 0]. Based on a figure in [28].

Nanostructured tungsten oxides are promising for various applications, such as gas sensing, hydrogen evolution, field emission or UV photodetection [31]. They are prepared by different strategies: direct growth from a tungsten surface at elevated temperatures (650–1300 °C) under the presence of very low concentrations of oxygen in an inert gas atmosphere, annealing WO_x in reducing atmospheres or vapour phase growth starting from WO_x source. Annealing WO_3/W substrate under hydrocarbon gas creates carbide between the layers which induces chemical-strain-driven nanowire growth [32]. In [33], oxidation of WS_2 powder on top of W film provided pine-tree-like arrays. The foil was heated to 1300–1400 °C in the presence of oxygen (10 Torr) and argon (490 Torr). The resulting morphology of the prepared tungsten oxide was the following: hollow fibres (outer diameter in micrometers, mm in length) consisting of $W_{18}O_{49}$ made up by multiple single crystal whiskers of 50 to 500 nm diameter. The hollow structure formation was attributed to heat dissipation.

Since the sub-stoichiometric compounds are often used as precursors for the synthesis of WS_2 due to their anisotropic shapes, the reduction series of small dimensional WO_{3-x} have been extensively analyzed [34]. The presence of water molecules enhances the growth of nanowhiskers. Volatile $WO_{3-x} \cdot nH_2O$ molecules are formed, later condense on the nanowhisker tip and are subsequently reduced. Many authors emphasize the role of water for whisker formation. Water, either an added gas or a product of reduction by H_2, enhances vapour transport of tungsten oxide [34]. In [35], it is suggested that hexagonal channels in $W_{18}O_{49}$ provide a path for the transport of tungsten oxide vapour along the growth direction [0 1 0].

In study [36], reaction $W_xO_y^- + H_2O$ was analysed. $W_xO_y^-$ clusters were generated using molecular beam valve source and water vapour was introduced into the system. Then, mass spectra was recorded at different temperatures. Reaction rates for reaction

$$W_x O_y{}^- + H_2O \longrightarrow W_xO_{y+1}{}^- + H_2$$

and

$$W_x O_y^- + H_2O \longrightarrow W_xO_{y+1}H_2^-$$

were compared as functions of temperature (range only 29–80 °C). The ratio of reaction coefficients for water addition to oxidation decreased with higher temperature. That means that at elevated temperature, molecular hydrogen is more likely to be formed. Hydrated $WO_2(OH)_2$ is very volatile and its presence could be important for gas phase growth.

Tungsten oxides in the form of whiskers undergo sublimation above 750 °C which acts as a barrier for the formation of nanowires longer than 1 µm. It is therefore necessary to employ lower temperature methods to prepare sufficiently long crystals with small diameters. Using W compounds such as W_2N reduces growth temperatures to 600 °C and longer nanowires are possible to obtain. Implating ions into WO_x thin films and annealing at 600 °C provides growth induced by local stress [37].

In reference [38], several µm long $W_{18}O_{49}$ nanowires with diameter of around 20–50 nm were synthesized at 600 °C from a fine tungsten powder at the presence of water vapour. The nanowires tend to form bundles when the initial particles are larger — see Fig. 2.7. It is not uncommon that the oxide nanowires form these log-like structures and they are a regular byproduct in sythesis of nanotubes. They sulfidize in the reactor slightly differently from separate nanowires [39].

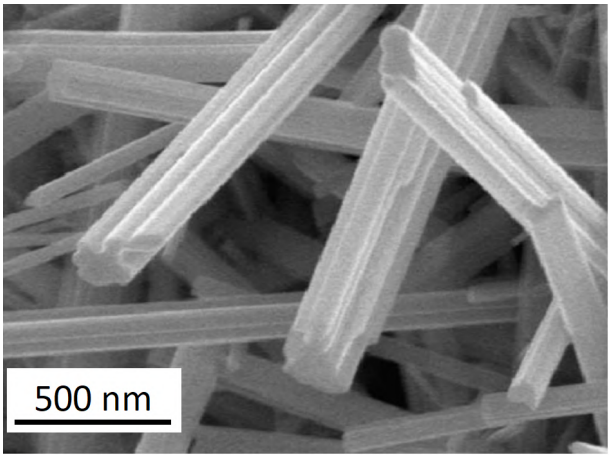

Figure 2.7: Bundles of $W_{18}O_{49}$ nanowires are a common product of oxidation of W particles about 0.6 µm in diameter. Image adapted from [38].

Strategies to further lower the reaction temperature to 500 °C, such as starting with defective metastable W structures, have been developed [40]. A deposited amorphous W with high oxygen content at the surface serves as the substrate for nanowire growth with diameters around 20 to 40 nm and µm lengths at temperatures higher than 450 °C. At 500 °C, there are nanoparticles of about 50 nm at the base of the nanowires (see Fig. 2.8) and the phase of the nanowires is $W_{18}O_{49}$. If the temperature is higher than 650 °C, wider tapered polycrystalline WO_3 nanowires are formed. By evaporation of tungsten powder, the lowest temperature for $W_{18}O_{49}$ whisker growth was achieved (350–450 °C) and the final nanowires exhibited diameters of 10–50 nm and lengths of around 1 µm. The presence of pre-oxide layer on the substrate was essential in this case for the nanowire growth [41].

An in-situ SEM observation of the growth process of WO_x nanowires was conducted in [42]. A tungsten film was heated to 660 °C and a nozzle located in the vicinity of the

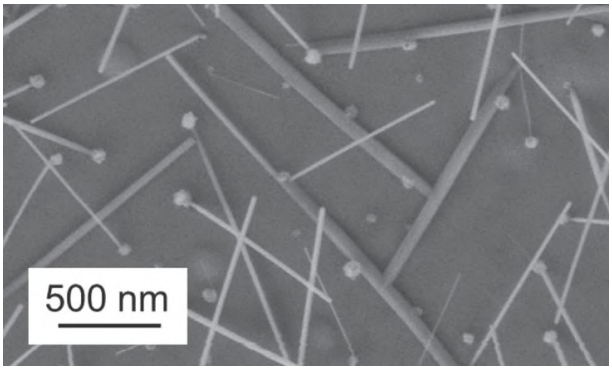

Figure 2.8: WO_x nanoparticles appear on the amorphous W surface with high oxygen content and from their facets, highly crystalline $W_{18}O_{49}$ nanowires develop, the temperature is 500 °C. Image adapted from [40].

sample served as a source of oxygen. The resolution was limited however. Some wires underwent broadening from their base when the reaction time was prolonged which is in agreement with previous ex-situ experiments. The lengths L (only in projection) were measured in time and the data were fitted as

$$L = L_0[1 - e^{-\frac{t-\Delta t}{\tau}}],$$

where L_0 is the terminal length, t is time, Δt the time when the nanowire started to grow and τ a time constant. The authors did not address the impact of e-beam of low energies on the reaction kinetics.

Quite interesting results were obtained when oxidizing W lamella on Mo grid in the presence of oxygen in an environmental TEM [43]. Real-time observations of growing $W_{19}O_{49}$ nanowires with atomic resolution demonstrated the domination of vapour-solid mechanism. The nanowires grew also on the Mo grid and the mechanism was described in the following way: the vapour is adsorbed on the substrate and the wire and the molecules diffuse toward the tip where it contributes to the growth of $W_{18}O_{49}$ due to the minimal surface energy. Figure 2.9 shows the lattice formation at the tip of nanowires. As to the time-dependent lengths of the nanowires, two regimes can be detected — at first, the lengths increase roughly linearly. When the WO_3 molecules seize to diffuse quickly enough to the tip (wire is longer than the diffusion length), the growth continues at a very low constant rate. The diameters of nanowires increased during their growths and the e-

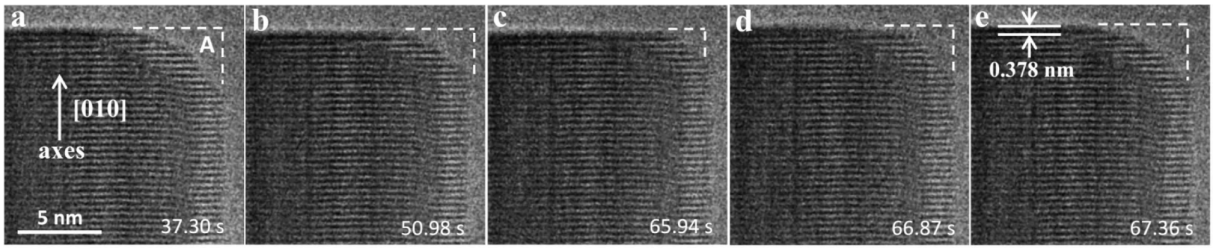

Figure 2.9: ETEM observation of the formation of new layers of $W_{18}O_{49}$ nanowires growing from W lamella heated in oxygen. In the real time atomic-layer-resolved imaging, precursor vapour molecules fill the rim and an almost flat facet is formed. Atoms diffuse from the corner to the growth front and leave the corner truncated again. Figure adapted from [43].

beam was found to perturb the reaction. For higher electron doses, there was a significant reduction of growth rate. At higher temperatures (tested range 700 to 1000 °C), more rapid growth was observed. The influence of oxygen pressure was studied in the article as well. Higher pressure resulted in higher reaction rate which strengthens the statement about vapour transport in comparison to surface diffusion. If surface diffusion of tungsten were the major mechanism for the elongation of nanowires, increasing pressure should not produce such dramatic changes.

Apart from the growth mechanism, electron beam damage in $W_{18}O_{49}$ nanowires was investigated in the reference [30]. 200 kV electron irradiation at 750 °C reduced the oxide nanowires to metallic tungsten. The dose rate was $3.2 \cdot 10^4$ C/(m^{2}s) [1]. O was depleted from $W_{18}O_{49}$ and the nanowire became thinner and bent. It was attributed to the core-hole Auger decay. No decomposition took place by simple heat treatment without electron irradiation below 850 °C and above this temperature, the $W_{18}O_{49}$ nanowires evaporated. The reaction pressure for both the growth and decomposition was 10^{-6} Pa. One of the oldest in-situ TEM observation of tungsten oxide wire bundles [44] deals with their decomposition as well. They grew the oxide at 10^{-1} Pa at very high temperatures (700–1300 °C) from tungsten filament and upon a prolonged exposure to the electron beam at 1100 °C, some segments of the crystals became thinner and eventually, they broke down at these weak points.

2.5. Analytical Description of Vapour–Solid Growth Mechanism

Nanowires can be synthesized by multiple methods: vapour–liquid–solid (VLS), vapour–solid–solid (VSS), non-catalytic vapour–solid mechanism, chemical vapour deposition (CVD) and others. Detailed observation of growth rates allows for an identification of limiting factors. Most of the analytic descriptions were done for VLS growth since it has been the most extensively studied one. During VLS, a liquid catalyst is supplied semiconductor material from vapour phase and a nanowire crystallizes from the supersaturated droplet. The mechanism is for example valid for Si nanowires growth with Au particle as a catalyst and SiH_4 gas as a precursor. First, SiH_4 is adsorbed on the Au—Si liquid and Si is incorporated within the droplet. At the same time, some silane and hydrogen are desorbed from it and Si nanowire nucleates. In VSS, a vapour phase provides material for a step-flow growth mode and the main difference from VLS is that for the solid catalyst, the adsorption of gases is more difficult and the atomic transport on the sidewalls plays an important role [45]. Analogous mathematical description of vapour transport along the wire can be applied to describe the problem illustrated in Fig. 2.10.

When mathematically describing some of the steps, the geometry is simplified and some approximations must be made. Firstly, the nanowire can be approximated as a cylinder

[1] For comparison with SEM doses: With current 100 pA (often used in this work) and scanning window 500×500 nm, the dose rate is approximately 40 C/(m^{2}s). Of course, the effect of 12 kV and 200 kV electrons is different but it is clear that the dose in the commented paper is much higher than those used in this work.

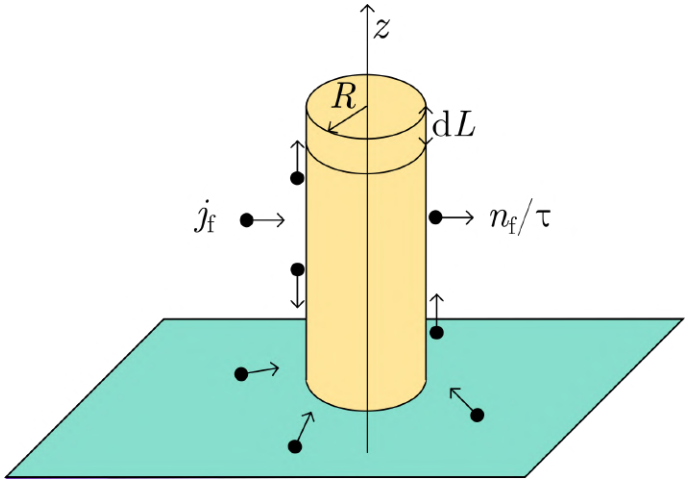

Figure 2.10: Coordinate system in a geometrical overview. All particles which diffuse towards the top of the wire contribute to growth.

for simplicity and secondly, the substrate is an infinite plane [2]. The equations will be for stationary state (time derivatives will be equal to zero).

The evaporation process is governed by Arrhenius type equation

$$k_e \propto e^{-\frac{E_A}{kT}},$$

where k_e is the evaporation rate, E_A the activation energy which takes into account all the steps needed (for example liquid to vapour energy change in VLS and desorption of vapour phase), k the Boltzmann constant and T temperature. Effectively, the evaporation rate determines the time that an adsorbed molecule or atom diffuses along the substrate and nanowire before it desorbs [3]. The adatom concentration n_s on the substrate is given by diffusion equation in polar coordinates

$$D_s \bigtriangledown^2 n_s - \frac{n_s}{\tau_s} + j_s = 0, \tag{2.1}$$

where D_s is the diffusion coefficient on the substrate (follows Arrhenius equation as well), τ_s is the effective lifetime of the adsorbate on the surface (inversely proportional to desorption rate k_e), j_s is the flux of incoming gas phase, $\bigtriangledown^2$ is the 2D Laplace operator in the substrate plane. A boundary condition is that the derivative of n_s is equal to zero for the radial coordinate $r \longrightarrow \infty$. The equation 2.1 needs not be solved, in the simplest case, we can only take a boundary condition for adatom concentration n_f on the wire's sidewall

$$D_f \frac{dn_f}{dz}\bigg|_{z=0} = -q, \tag{2.2}$$

where q is the flux equal to the amount of adsorbed vapour coming from the substrate to the base of the wire through a unit-sized part of a circumference and D_f is the diffusion

[2]The situation is more complex in this work as the substrate is replaced by nanotubes or platelets. The mathematical description is only informative here and serves as a guide for identifying rate-determining factors.

[3]Based on information from section 2.2, it is necessary to consider the effect of the electron beam here. If the irradiation influences diffusion rate or desorption in any way and therefore changes the diffusion length, it is going to have either a detrimental or beneficial effect on the subsequent growth.

coefficient on the nanowire's sidewall. This approach has another advantage — we can plainly describe the flow of material towards the wire without the need to describe the geometry below it. We merely create a lower boundary condition for the concentration flux.

The one-dimensional adatom concentration n_f on the sidewall facets of the nanowire is given as

$$D_\mathrm{f}\frac{\mathrm{d}^2 n_\mathrm{f}}{\mathrm{d}z^2} - \frac{n_\mathrm{f}}{\tau_\mathrm{f}} + j_\mathrm{f} = 0, \tag{2.3}$$

where z is the vertical axis coordinate, τ_f is the effective lifetime on the sidewall and j_f is the flux of incoming gas phase on the facets.

Equation similar to 2.3 would be valid for the small growth front if we wanted to obtain concentration n on it, only the situation is more complex since the nucleation of new layers takes place here. The easiest way to look at the problem is to assume a boundary condition at the rim of the end facet of the nanowire — it is treated as a sink for the incoming material. That can be written as

$$n_\mathrm{f}(z = L) = 0, \tag{2.4}$$

where L is the length of the wire. Any vapour which lands on the growth front contributes to the growth and, if it is the amount of material which limits the growth rate, the rate obtained by previous equations will only be lowered by a small constant.

Now, we have two boundary conditions 2.2, 2.4 for a second order differential equation 2.3. Of course, the boundary conditions chosen for this calculation will provide an inaccurate description if anything but the amount of vapour molecules is the limiting factor. Any other approaches based on minimal energies and non-stationary equations would be much more complex and beyond the scope of this thesis.

The expression for growth rate of the nanowire of length L can be written as

$$\frac{\mathrm{d}L}{\mathrm{d}t} = -\frac{2D_\mathrm{f}V_0}{R}\left.\frac{\mathrm{d}n_\mathrm{f}}{\mathrm{d}z}\right|_{z=L}, \tag{2.5}$$

where V_0 is the volume which is occupied by one vapour molecule and R is the radius of the nanowire. Let $\lambda = \sqrt{D_\mathrm{f}\tau_\mathrm{f}}$ be the diffusion length. Equation 2.3 yields

$$\left.\frac{\mathrm{d}n_\mathrm{f}}{\mathrm{d}z}\right|_{z=L} = -\frac{q}{D_\mathrm{f}}\operatorname{sech}\left(\frac{L}{\lambda}\right) - \frac{j_\mathrm{f}\sqrt{\tau_\mathrm{f}}}{\sqrt{D_\mathrm{f}}}\tanh\left(\frac{L}{\lambda}\right). \tag{2.6}$$

If we combine equations 2.5 and 2.6, we obtain a formula describing rate as a function of length

$$\frac{\mathrm{d}L}{\mathrm{d}t} = \frac{2V_0 q}{R}\operatorname{sech}\left(\frac{L}{\lambda}\right) + \frac{2j_\mathrm{f}\lambda V_0}{R}\tanh\left(\frac{L}{\lambda}\right). \tag{2.7}$$

An implicit formula for length can be than derived by integration of an rearranged equation 2.7

$$t = \frac{R}{2j_\mathrm{f}V_0}\ln\left[1 + \frac{\lambda j_\mathrm{f}}{q}\sinh\left(\frac{L}{\lambda}\right)\right]. \tag{2.8}$$

It can be seen that for $j_\mathrm{f} = 0$, the solution changes to

$$t = \frac{R\lambda}{2qV_0}\sinh\left(\frac{L}{\lambda}\right). \tag{2.9}$$

Now, we can write $L(t)$ as

$$L(t) = \lambda \operatorname{arcsinh}\left\{\frac{q}{\lambda j_\mathrm{f}}\left[\exp\left(\frac{2 j_\mathrm{f} V_0 t}{R}\right) - 1\right]\right\} \tag{2.10}$$

and for $j_\mathrm{f} = 0$, we obtain

$$L(t) = \lambda \operatorname{arcsinh}\left(\frac{2 V_0 q t}{\lambda R}\right). \tag{2.11}$$

Time derivative of formula 2.10 or 2.11 then describes the growth rate. A qualitative analysis of adatom concentration profile along the wire is illustrated in Fig. 2.11 and calculated growth rates are depicted in Fig. 2.12. These findings will be later used for fitting experimental data in section 4.3.

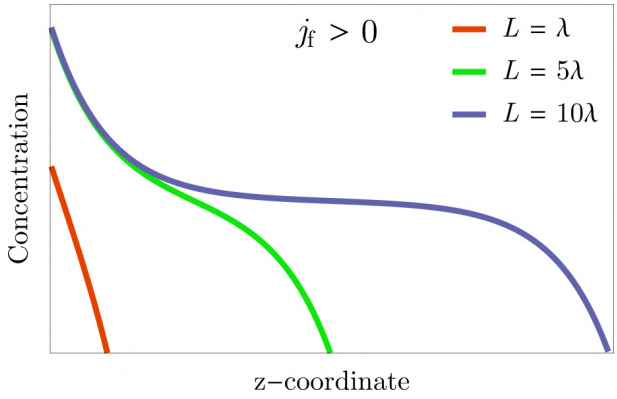

Figure 2.11: Concentration profile along the wire for non-zero flux j_f. For lengths larger than λ, we observe three regions: abrupt decrease of concentration due to a finite diffusion length, almost constant concentration as a result of no consumption of the material and a rapid decrease due to the growth. In the middle segment, the desorption is exactly compensated by flux j_f and an equilibrium concentration $n_\mathrm{f} = j_\mathrm{f} \cdot \tau_\mathrm{f}$ is established.

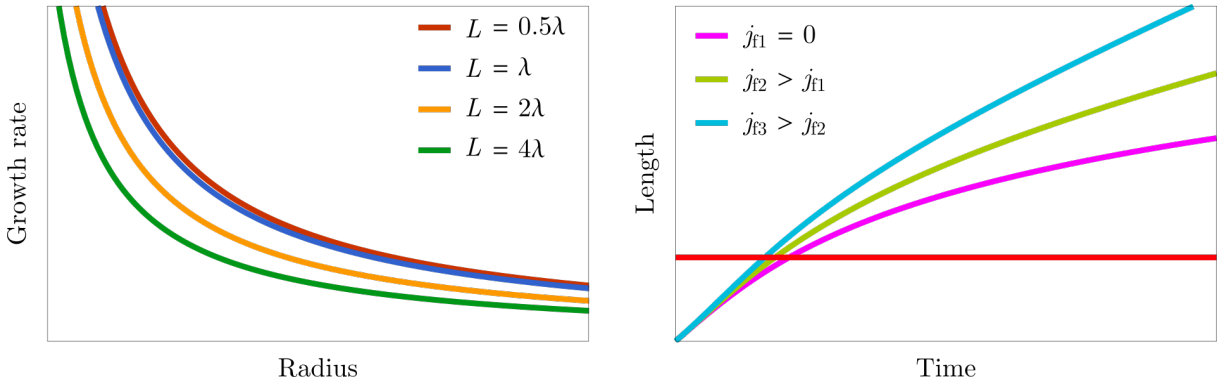

Figure 2.12: Left: Growth rate as a function of wire's radius plotted for different lengths of the wire. Since the surface of the growth front is proportional to r^2 and the surface of the facet only increases with r, the higher is the radius, the lower is the growth rate. Right: Calculated lengths of wires in time for three fluxes j_f. At the beginning, there is not much surface for the vapour to land on and all material is supplied through the base of the wire. Red line marks the diffusion length.

3. Methods

3.1. Instrumentation

A miniaturized μReactor for in-situ SEM experiments was utilized for the study of reaction rates (see Fig. 3.1). The SEM used was Thermo Fisher Helios G5 and the vast majority of imaging was done in the immersion mode. A pressure-limiting aperture ensures that the gas injected into the reactor area does not substantially increase the surrounding pressure and an operation of the microscope is in standard high vacuum mode. The possible overpressure is up to 100 Pa. Additionally, STEM imaging is an option for the thinner areas of the chip if a reactor with an aperture below the chip is used.

A heating MEMS element (NanoEx), which can be used in TEM with a special holder, was used as a substrate. The main advantage is that the calibrated chip alters the heating power when the gas which would cool the chip down is added (Pirani gauge-like effect). It is possible to heat the sample up to 1200 °C with an approximate error of 4% [47] if there is no gas injected. The heating takes place mostly in the centre of the chip and the stage remains at room temperature and as a result, thermal drift is minimized. It is also possible to apply an external electric field to the analysed sample in order to study its ferroelectric or piezoelectric properties but it was not relevant for the presented work.

It is however necessary to mention limitations associated with utilizing the system described above. Firstly, the temperature changes slightly along the chip. In the central area, the temperature should vary below 1% if there is no gas in the surrounding [47]. In case a gas flux is present, the situation can be different. We conducted a temperature calibration experiment with a temperature sensitive paste which proved that it can vary significantly even within the heated region of the chip if water vapour is introduced (estimated error 10%). The paste itself changes the heat transport but in the very center of the chip, the paste melted when temperature was set to 610 °C which should happen at 621 °C (only different by 2 %). In order to minimize potential errors in temperature reading, the experiments which are meant to describe growth kinetics were always situated in the centre of the chip.

Another, and perhaps the most prominent problem, is the control over local pressure in the reactor. The amount of gas going through the inlet and the diameter of the pressure limiting aperture are not the only factors which determine the final pressure of gas in the reactor but more importantly the flux. The working distance is a strongly influencing

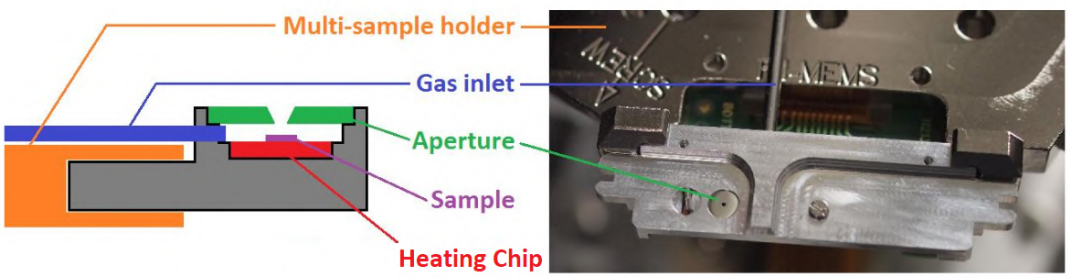

Figure 3.1: A schematic of μReactor in the SEM with upper aperture only. Introduced gas is mainly restricted to the area below the limiting aperture. Image adapted from [46] and edited.

factor since the space near the objective pole piece is pumped down. The change of heating power when the gas was added served as a way to estimate the local overpressure. Because of all these factors, the pressure for all experiments in the reactor can only be listed in orders of magnitude.

Some experiments were conducted in SEM in low vacuum mode where the pressure is measured with a higher precision since the gas occupies the whole chamber. The main issues with this set-up are a limited resolution, sample drift and upper limits of the water pressure which can be introduced into the chamber. For the final experiments, another type of reactor was used. It has two parts — top aperture with a gas inlet which can be retracted similarly to Gas Injection System and a standard heating MEMS stage below.

3.2. Kinetics of Tungsten Oxide Growth

In the presented work, tungsten disulfide nanotubes and platelets are exposed to water vapour at elevated temperatures and their oxidation is studied. The original assumption was that the oxidation would proceed from the outer layer or in some inverse analogy to the conversion of oxide crystals to tungsten disulfide nanotubes (briefly described in section 2.3). The initial experiments revealed that the process is rather complex and different from all predictions. The nanotubes were decorated with oxide nanoparticles and nanowires while their overall structure was generally preserved until later stages of the reaction.

In order to describe the whole reaction mechanism, identification of intermediate phases, diffusion pathways as well as the rate-limiting processes, and the determination of possible catalytic mechanisms are necessary. One of the aims of the thesis are to describe whether the electron beam influences the oxidation in any way.

The nanotubes and platelets[1] were dispersed in isopropylalcohol (IPA) and ultrasonicated for a few minutes to ensure that they do not agglomerate too much. A droplet of such dispersion was put onto the thin center of MEMS chip and I waited until the droplet dried out. The chip was then loaded into one of the used holders and heated in SEM vacuum (pressure in the order of magnitude of 10^{-3} Pa) to 350 °C. For the experiments, it was necessary to find a few separate nanotubes and that was achieved almost every time without much effort. IPA was a significant contaminant and annealing at elevated temperatures ensured that any remains of the solvent evaporated. When continuous electron beam scanning seized to create contamination layers (usually within 20 min of heating), water vapour was introduced. The amount of water was such that at 350 °C, the increase of heating power was about 10 %. That corresponds to amounts of 10^0–10^1 Pa in the reactor based on previous calibrations. Of course, this is dependent of the base pressure which varied due to the state of the microscope (time of being vented before, change of stages, etc.) but it was always in the range of $8{\cdot}10^{-4}$ Pa to $5{\cdot}10^{-3}$ Pa at the beginning of the experiments. Then, the heating power was increased to the target temperature. Since we wanted to see what exactly the role of water is apart from providing oxygen, we conducted a few experiments with CO_2 and O_2/air mixture[2] as oxidative atmospheres.

[1] WS_2 nanotubes used in this work were prepared by the slow diffusion-controlled sulfidization of tungsten oxides briefly described in section 2.3 in the group of prof. Alla Zak. Platelets were bought from Alfa Aesar.

[2] It was intended to perform the reaction in O_2 but, as was found out later, the inlet of gas had a leak during the experiment. A presence of a small amount of water is therefore expected.

As to the imaging, the accelerating voltage was chosen as 12 kV (and kept for all experiments so that one variable was eliminated) and the current was 100 pA. There was not much freedom since significant charging effects were present. Lower voltages lead to a worse spatial resolution. Introducing water vapour reduced these a lot but some imaging was done in vacuum and it was convenient to have optimal settings for all conditions. Dwell times and number of pixels were chosen to reflect the reaction speed. Usually, images containing 1536×1024 pixels were recorded for the sequences with 10 µs dwell time per pixel. Such conditions meant 16 s per frame and quality of the data was sufficient for further analysis when the dimensions of the scanning windows were below 1 µm. The only process which was usually too fast to be recorded with these imaging parameters was the formation of nanoparticles. Since the wires grow in different directions, the measured lengths were just projections. The solution was tilting the chip and finding the angle under which the projection is longest. Ex-situ imaging under different tilts and rotations was not an option, without heating, contamination was too severe and the chip must be placed in a special holder if heating is required. The solid angle from which one can obtain a decent in-lens signal is given by the geometry of the viewing aperture in the holder. Later, a new version of the holder (separate insertible upper lid with an aperture and plain heating stage) became available to me. It was therefore possible to oxidize the nanotubes first and afterwards obtain the real angles contained by the created wires and the substrate. Direct measurement of lengths would introduce additional error since the reaction is first slowed down by lowering temperature and then terminated by closing the water inlet and during this time, the wires can slightly elongate. Still, the uncertainty in determining the actual angles α under which the wires grow is significant, here estimated as $\pm 10°$. The error in length ΔL then is a function of angle since L is proportional to $1/\cos\alpha$.

3.3. Determination of the Extent of Oxidation in WS_2 Nanotubes

SEM observation of the oxidation reveals a lot about the dimensions of nanowires and nanoparticles in time, but small changes within the original nanotube remain undetected. Ex-situ TEM imaging and spectroscopy should be able to detect them but there are some arising problems. Almost with no exception, the nanotubes start to oxidize in the parts closest to the substrate, and so free standing nanotubes lying in part on Mo TEM grid do not represent the experiments well enough. It would be advantageous to put the whole MEMS chip into a TEM holder since some parts of the chip are comprised of a thin enough silicon nitride membrane but no holder was available to me. The next idea was to cut out a part of the MEMS chip and place it onto a TEM grid but this proved to be a dead end. Material re-deposition during FIB milling was a major problem and so, the only other viable option was FIB cross sectioning. This is slightly more time-consuming than the previous ideas but it produced some decent results.

The lamellas were prepared using Thermo Fisher Helios G3 660 dual beam at CEITEC Nano facility. First, such nanotubes were selected, which (according to SEM imaging) seemed to lie on the substrate without crossing with other tubes. Then, carbon FEBID (focused electron beam induced deposition) under tilt of $\pm 25°$ was used to cover the nanotube from both sides. In case this process was omitted or not done properly, holes formed around the nanotube and some of its parts were milled preferentially.

Then, carbon FIBID (focused ion beam induced deposition) produced a very thick (3 µm) covering layer for the lamella. The rest of the cross sectioning process was exactly the same as for a standard lamella fabrication. If the previous EBID layer was not sufficient (at least 200 nm on top of the nanotube), ion beam deposition disrupted the upper layers and the nanotube was deformed or collapsed. Due to the inhomogeneity of the carbon cover layer, the lamellas were sometimes brittle as well due to being slightly thicker in the area of the nanotube. Apart from that, no greater difficulties arose.

Such fabricated lamellas were imaged with Thermo Fisher Titan Themis with an image C_s corrector at the accelerating voltage of 60 kV to avoid as much knock-on damage as possible. STEM EELS and EDS were used to identify the oxygen and sulfur content.

4. Results

4.1. General Information about the Process of WS_2 Oxidation

Tungsten disulfide nanotubes undergo a lot of changes when exposed to water vapour at elevated temperatures. These alterations start to happen quickly enough at around 400 °C so all real-time experiments were conducted at temperatures from 400 to 750 °C[1]. The amount of defects on the nanotube prior to the experiment plays a significant role as any defected areas such as open ends or edges of outer sheets are the first locations to be oxidized. Within a few minutes, a small change in SE contrast along the nanotube can be detected which is caused by the formation of a thin nonuniform layer of tungsten oxide. Over time, these areas begin to coalesce, which is easily observable below 500 °C but quite abrupt above that temperature. Small particles are formed after a short while and these often lie in lines such as in Fig. 4.1. Their directions are probably related to the directions in which the first WS_2 layer is folded. This is in correspondence with observation of grain boundaries in WS_2 monolayer becoming visible when slowly oxidized [27].

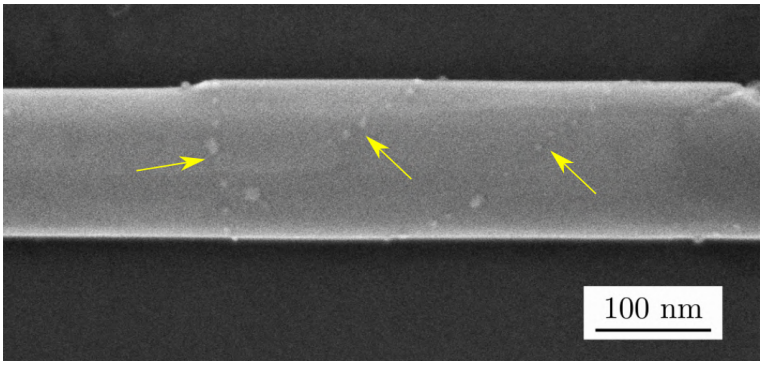

Figure 4.1: SEM micrograph showing oxide particles lying along lines which reveal chiral angles. These are formed within first minutes even at temperatures as low as 300 °C in 100 Pa of water vapour.

At $T < 450$ °C and without irradiation, nanoparticles are afterwards slowly formed along the whole nanotube. Some of them migrate or merge with others. They are presumed to be liquid WO_3 based on ex-situ TEM observation and XPS (X-ray photoelectron spectroscopy) measurement (Fig. 4.2). In TEM, their crystal structure is different for each cooled nanoparticle (but they are not amorphous). They do not disrupt interlayer distances of the nanotube as can be seen in Fig. 4.3.

From the nanoparticles, WO_x nanowires can start to nucleate and then rapidly elongate in one dimension because on the tip, chemical potential is smallest and 1D growth is

[1]Description of different reaction regimes often suffers from vague terms 'higher' or 'lower' temperature. The main issue is that the reaction progresses at different rates based on the initial state of the nanotube and also all previous exposures to water vapour at elevated temperatures. There is a significant difference between a tube which was first exposed to 400 °C for 20 min and then heated to 500 °C for 20 min and a second one which was just heated to 500 °C for 20 min, which can be a problem if two experiments are conducted on the same MEMS chip. Overall, the processes described here had only progressed at different rates but the reaction products apart from the particles were the same.

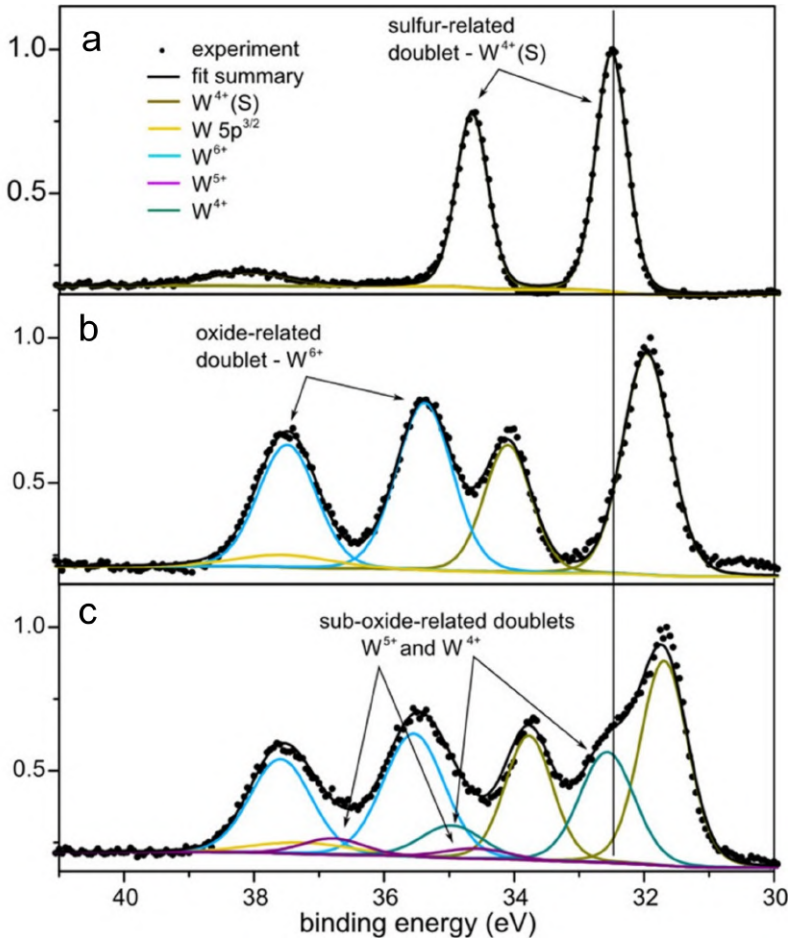

Figure 4.2: 4f peak of W measured by XPS on (a) pristine nanotubes (if they are annealed (550 °C) in vacuum ($5 \cdot 10^{-4}$ Pa, W peak looks identical thus proving no oxidation takes place), (b) nanotubes oxidized at 400 °C (additional dublet characteristic for W^{6+}) - WO_3 phase corresponding to the particles, (c) nanotubes oxidized at 510 °C (apart from W^{6+}, W^{4+} and W^{5+} dublets are present, which suggests the presence of substoichiometric oxide). The measurement using Kratos AXIS Supra was performed by Miroslav Kolíbal and more details can be found in [48].

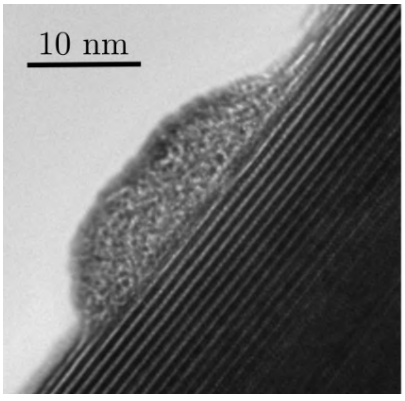

Figure 4.3: TEM image showing that the presence of nanoparticle does not alter interlayer distances of the nanotube, measured by Lukáš Kachtík.

therefore more energetically favourable than general isotropic growth of the crystal. If nanowires start to grow and the temperature is around 420 °C, they lie along the nanotube which is in contrast to the high-temperature case in which the wires stick out from it. When they share a part of the facet with the nanotube, their surface area is reduced which is energetically favourable as well.

Nanowires can be rapidly obtained from the nanoparticles either by increasing temperature (Fig. 4.4) or by e-beam irradiation. As the wire grows, the nanoparticle is usually consumed (Fig. 4.5). As the particle shrinks, the nanowire can change the angle it makes with the axis of the nanotube. In some cases, the particle remains the same in size but the wire already stops growing. It can be a nucleation base only and then be in the middle of a wire elongating at both ends (Fig. 4.6).

In case the tungsten oxide droplet exceeds a certain size, no nanowires start to emerge from it even if the temperature is elevated afterwards. That can be explained by a simple idea — a small nanoparticle has higher vapour pressure due to its larger curvature so it can easily promote the formation of nanowires. However, it is possible to use electron beam irradiation to rapidly convert the big ones into small elongated crystals which lie along the nanotube.

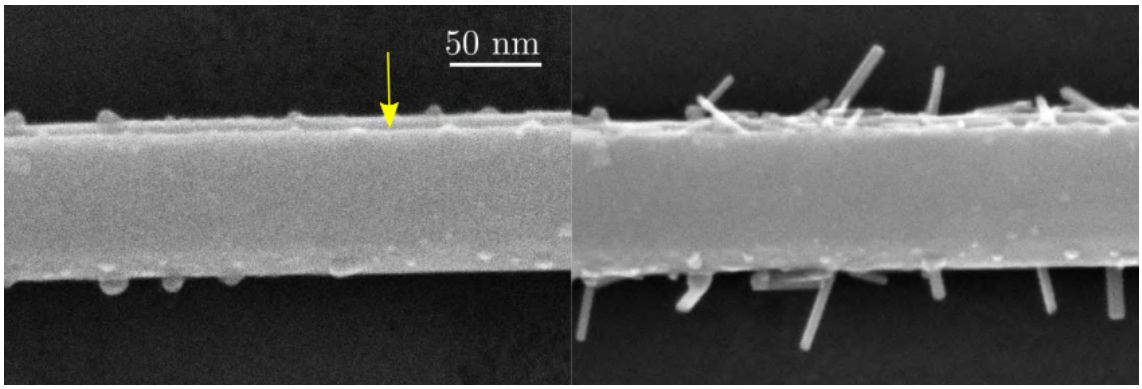

Figure 4.4: Nanowires nucleate from small enough nanoparticles. First, large nanoparticles were formed without irradiation at 470 °C (left) and nanowires were obtained by increasing temperature to 520 °C and scanning over the nanotube (right). There are most likely two nanotubes lying on each other (edge of the upper one is marked by an arrow) and it is mostly the lower one from which wires emerge.

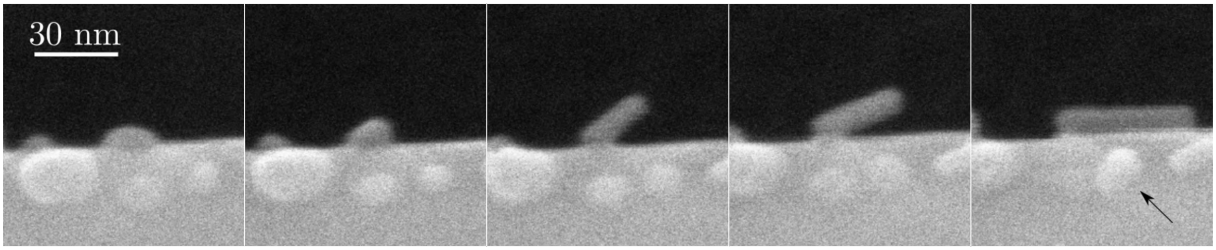

Figure 4.5: A complete conversion of nanoparticle into wire followed by the wire changing the angle it makes with the nanotube. Additionally, we can observe that two smaller particles right below the wire merge. Time between consequent images is approximately 50 s, temperature 550 °C.

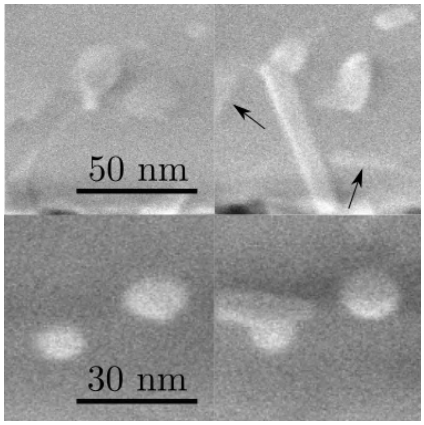

Figure 4.6: A detailed image of conversion of nanoparticles into wires. Top: The nanoparticle's size is reduced as the wire nucleates. The wire first starts as very thin and widens during the first seconds of growth. Additionally, WS_2 layer is consumed slightly in the process (arrows). Bottom: Nanowires can grow at both ends and have a nanoparticle in the middle.

When the temperature is higher than 450 °C and the beam assists the reaction, nucleation of nanowires is quicker and more frequent. Their diameters are larger and usually, there are no nanoparticles at their base. In the SEM, we are usually able to clearly see oxide droplets as small as 3 nm so it is unlikely that their existence underneath a wire would remain undetected unless the creation of a nanoparticle and nucleation of nanowire of same diameter happened between two scans. Most of the nanowires start growing from the lower side of the nanotube close to the substrate, which prevents the observation of their bases so it is difficult to say which conditions yield only nucleation from nanoparticles. Additionally, the wires are thinner and shorter when they grow from the top of the nanotubes. This is illustrated in Fig. 4.7. It is unlikely that this would be due to a nonuniform temperature on the nanotube because the substrate which is heated is very large in comparison to the nanotube.

As the reaction temperature increases (e.g. 550 °C), wires occasionally tend to widen. At the base, new crystals sharing a part of their facet with the original nanowire start growing (Fig. 4.8). When that happens, the original wire almost seizes to grow and only continues after the neighbours reach its length. That suggests that the most prominent source of molecules comes from the base. They are consumed by the shorter wires. Based on these findings, vapour–solid growth seems to be the most logical mechanism. The wires often form bundles like that [39] so this effect is not surprising.

Lukáš Kachtík performed TEM imaging of the nanowires, one of such images is shown in Fig. 4.9. Their stoichiometry has not been identified with certainty so far because W–O system is very complex and a huge amount of metastable phases have been reported. Most WO_x nanowires investigated in literature are $W_{18}O_{49}$ or $W_{20}O_{58}$ and grow in [0 1 0] direction and the corresponding interlayer distances in the growth direction should be 3.8 Å [30]. EDS measurement of W:O content provided an approximation of $WO_{2.9}$. One of STEM images (Fig. 4.9) shows a nanowire which indeed has interlayer distances 3.8 Å along the growth direction. It is likely that we can obtain different stoichiometry based on reaction conditions.

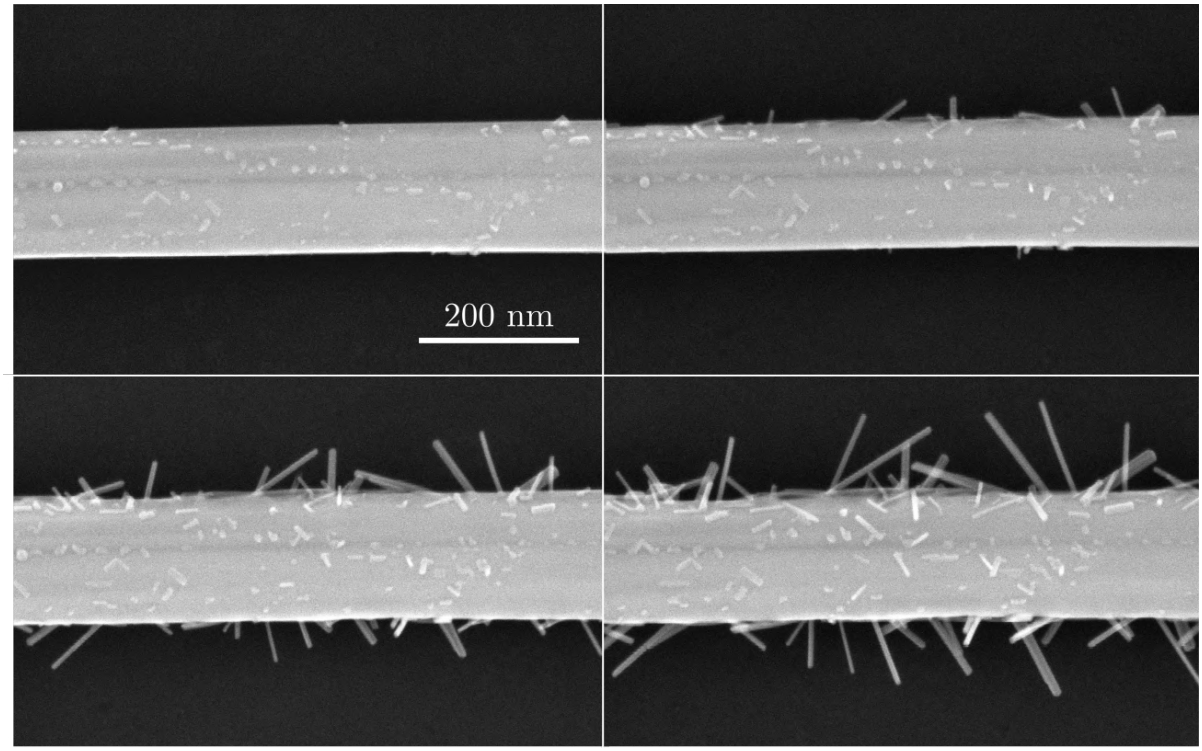

Figure 4.7: A series of SEM micrographs showing different growths on various parts of the nanotube. The thickest and longest wires emerge close to the substrate and the upper part of the nanotube is covered with thin short wires which is apparent even under tilt. It can be explained by these possible mechanisms: high SE yield which can possibly influence the growth and local increase in precursor vapour concentration due to the presence of substrate along which a lot of molecules can be transported. This particular nanotube was oxidized in at a wide range of temperatures in an experiment presented in section 4.3.2 where the lengths in their projections were measured. Time between each image is 3 min.

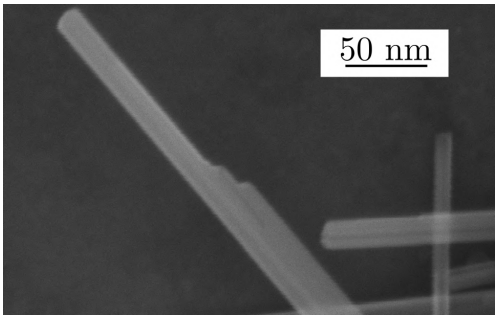

Figure 4.8: A step-like widening of the nanowires at higher temperatures ($T = 600\,^{\circ}\mathrm{C}$). The longest one waits for its neighbours to reach its current length and only then starts to rapidly elongate again. If the wires grew from the bottom, it should not make a difference that some of the wires are shorter. If they grew by vapour–solid mechanism, the concentration profile along the longest crystal would be affected by the consumption of the molecules by the adjacent wires and so its growth rate would rapidly decrease, which is indeed happening.

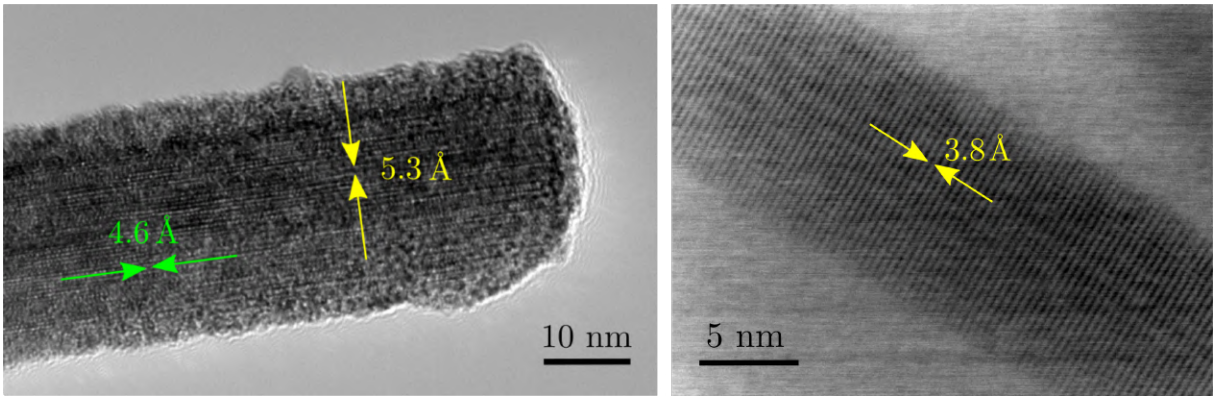

Figure 4.9: Left: TEM image of a nanowire with marked characteristic interlayer distances. The crystal has a lot of defects and the sidewalls are corrugated. Identification of the exact stoichiometry has not been achieved yet. Right: STEM image of a nanowire with interlayer distances corresponding to $W_{18}O_{49}$ or $W_{20}O_{58}$ growing in [0 1 0] direction. Images taken by Lukáš Kachtík.

Apart from WS_2 nanotubes, oxidation of platelets was tested, too. All curvature effects are suppressed and the wires start to grow from areas with the highest concentration of dangling bonds — defective prismatic edges (Fig. 4.10). If temperature is increased to 600 °C, the whole surface is conversed into a net of long nanowires (Fig. 4.11).

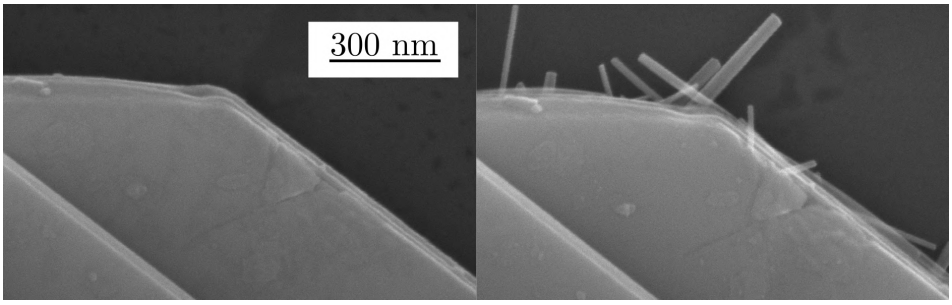

Figure 4.10: Left: A platelet lying on the substrate before oxidation. Right: The same platelet after an exposure to water vapour (irradiated for 8 min at $T = 500$ °C, pressure 5 Pa.). The first wires emerge from its edges.

As to the role of water, it attacks W–S bonds which leads to the exchange of S to O in WS_2 (expected byproducts would be SO_2 or H_2S). The oxide then clusters and forms WO_3 nanoparticles. Since water can form hydrogen and hydroxyl radicals (assisted by elevated temperatures and irradiation by electron beam), hydrogen can then reduce the oxide. Additionally, vapour transport of tungsten trioxide is enhanced by water [34] and hydrated complexes $WO_{3-x} \cdot nH_2O$ are most likely formed. When the reaction temperature is kept but the inlet of water is closed, crystals (e.g. 30 nm) of oxide (most likely WO_3 but this is only a speculation so far) are abruptly formed in the irradiated area which is most likely the consequence of disabling vapour transport of such complexes. Their size decreases further from the nanotube (Fig. 4.12).

If there is indeed H_2S present as a byproduct of oxidation, it could react with the surface of the WO_x crystal and cause monolayer WS_2 encapsulation of the nanowire [24]. Because EDS does not provide reliable information when the concentrations of the measured ele-

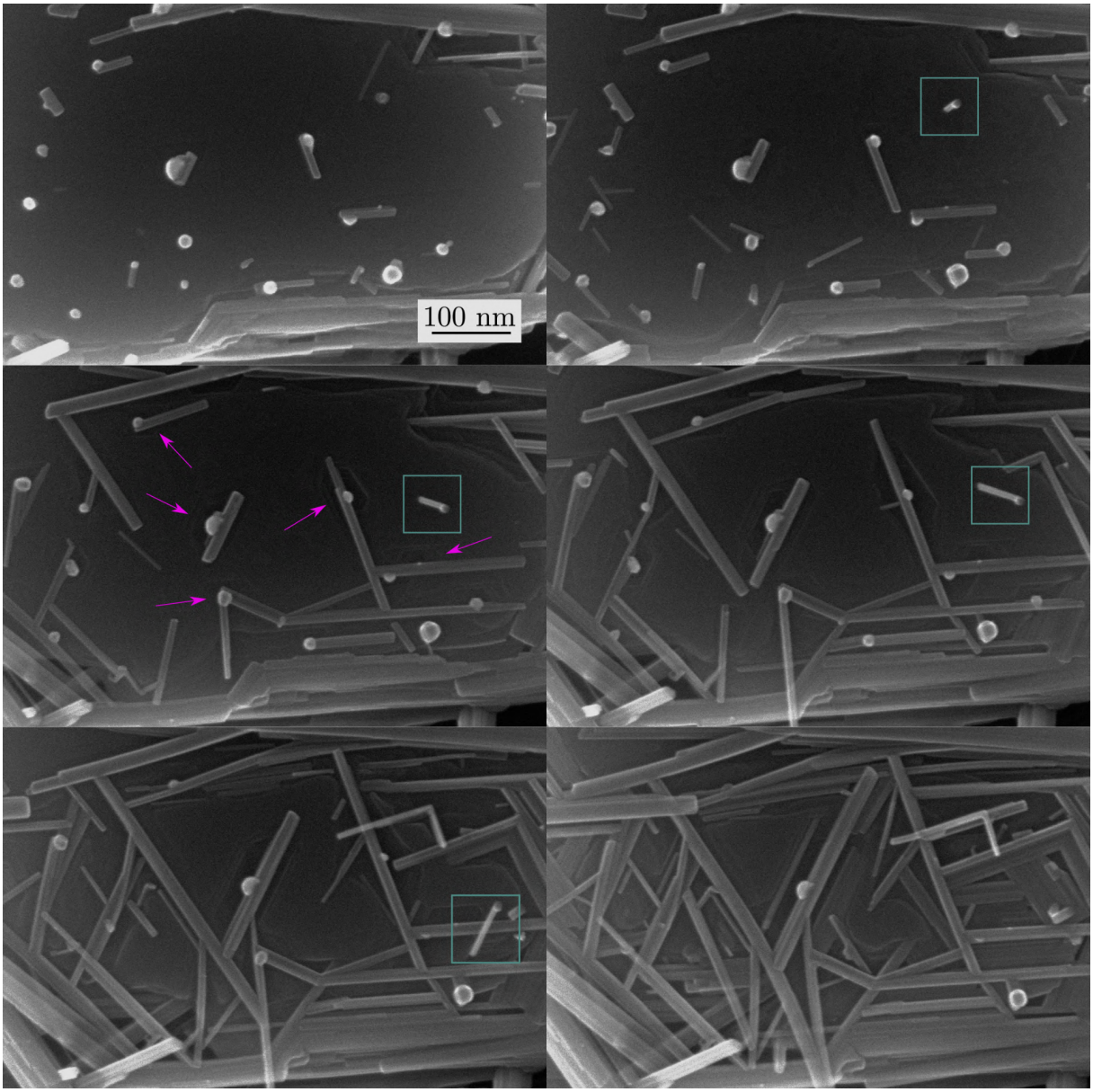

Figure 4.11: Conversion of the surface of a platelet into a network of nanowires. Arrows show areas under some of the particles, which were etched as the nanowires grew. For platelets, this effect is easily observable in contrast to nanotubes, where it is seldom clearly visible. Nanowire emerging from the nanoparticle marked by a blue square moves along the platelet and reflects from any defects it encounters suggesting that the nanoparticles truly are liquid. The sequence captures 30 min of the reaction. For the first four images, temperature was 600 °C, the last two 650 °C and the pressure was 5 Pa.

ments are low, we employed EELS measurement which provides better localisation than EDS as well. No sulfur signal was detected in the nanowires and so the hypothesis was dismissed.

To test the key role of water, we tried to use CO_2 and O_2 atmospheres which should be able to oxidize the nanotubes but not support the growth of wires since no hydrogen, which reduces oxide particles, is produced during the reaction and without water, no volatile clusters are formed. With O_2, nanowires were obtained analogously to H_2O atmospheres.

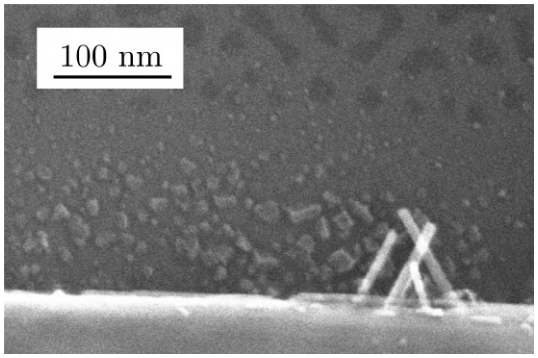

Figure 4.12: When water inlet is closed, small tungsten oxide crystals cover the nearest area around the nanotube.

As was later found out, we had a leak in the system and so water was present anyway. With CO_2, nanoparticles were formed but no nanowires emerged from them even after several hours of exposure at a wide range of temperatures (400–600) °C. Only under an intensive irradiation, some elongated crystals were formed (Fig. 4.13). Their morphology was different from what can be obtained in water and they formed abruptly in units of seconds between two scans and no longer elongated afterwards. The electrons most likely caused a decrease in oxygen concentration in the particle and it then transformed into a substoichiometric oxide. Both experiments need to be repeated to verify this hypothesis and a precautions must be taken to ensure there is truly no residual content of water.

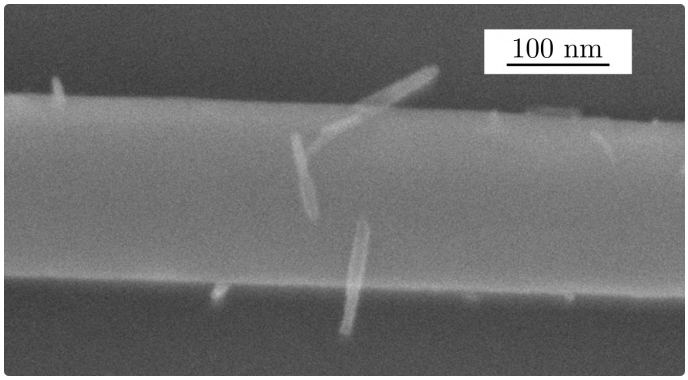

Figure 4.13: Wires obtained by oxidation in 50 Pa of CO_2 at 520 °C under intense irradiation for 2 hours. The wires have a different morphology than is usual for H_2O vapour and originate from nanoparticles by a rapid conversion initiated by the beam.

One more topic must be addressed — in most of the SE images, we can clearly see small variations of contrast along the substrate in the vicinity of nanotubes. Since we assume that volatile $WO_{3-x} \cdot nH_2O$ clusters are formed and they diffuse along the nanotube, there is no reason to believe that they should not reach the substrate as well. Interestingly, in rare cases, the oxide can even form thicker nonuniform islands from which some wires can even emerge (Fig. 4.14). Their morphology is identical to that of the wires growing from the nanotube and their formation is most likely caused simply by a local increase in concentration of volatile oxide.

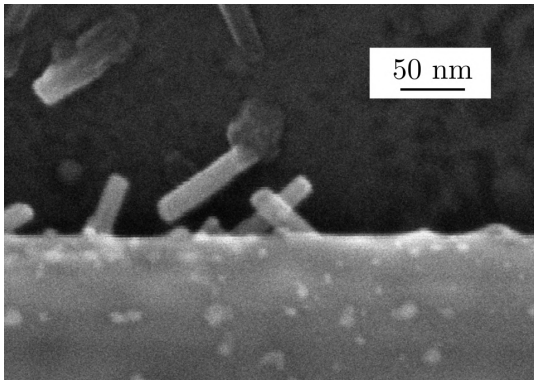

Figure 4.14: Wires growing from thick accumulated oxide layers on the substrate at 550 °C and pressure 5 Pa. The conditions in this particular experiment did not differ from the rest and the process is probably connected to the state of nanotubes prior to the experiment.

4.2. Measured Elongation of Nanowires

As the first quantitative real-time experiment, we decided to observe evolution of lengths in time for typical experimental parameters. No nanoparticles were detected at the bases of nanowires so the the curves should not be influenced by additional root growth. Since the nanowires grow in different directions, the only way to measure their length with at least some precision in SEM is to tilt the sample after the reaction finishes and find maximum projections, which is a lengthy process and it was done only for a few experiments. As it turns out, it brought little new information. For a given nanowire, the rate is merely multiplied by a constant which is not important for analysis of the shape of $L(t)$ curve.

The vapour–solid model derived in section 2.5 gives a function $L(t)$ which can be used for fitting. In the approximation of negligible molecular flux on the sidewall, the only material which contributes to the growth comes from nanowire's base and the function we obtain is

$$L(t) = \lambda \operatorname{arcsinh}\left[\frac{2V_0 q(t+t_0)}{\lambda R}\right].$$

Since the time of nucleation and first observation can be different, constant t_0 is added. It is logical to assume that the majority of the molecules comes from the base of the nanowire because the oxide is formed along the nanotube and can freely diffuse along it. Equation 2.10 gives a poorly conditioned fitting problem which suggests that j_f is very small.

The function describes our experimental data surprisingly well (measurements at two different temperatures are in Fig. 4.15 and 4.16).

Obtained coefficients c_1, c_2 and c_3 combine parameters λ, q, t_0 and projection angle α so it is not possible to extract values of λ and q which would be desirable. Therefore, the next step was to measure real lengths to eliminate the projection angle (Fig. 4.17 and 4.18). Extracted characteristic parameters describing the growth rate are in Table 4.1. From them, we can conclude that individual nanowires are strongly influenced by their position on the nanotube and direction of growth as these are connected with the e-beam effects as well as local flux of molecules contributing to the growth. Diffusion length can be estimated in orders of magnitude but that is the only information we get.

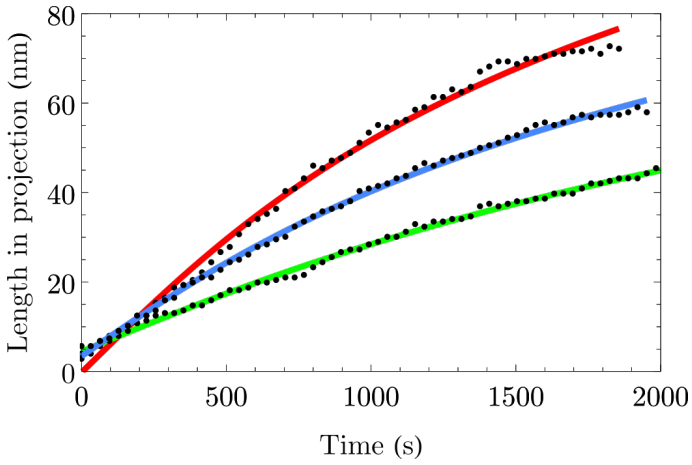

Figure 4.15: Measured and fitted evolution of lengths in time at 450 °C. The function used for fitting: $L = c_1 \cdot \operatorname{arcsinh}(c_2 t + c_3)$. The parameters do not give much information about q and λ but the fit copies the data very well.

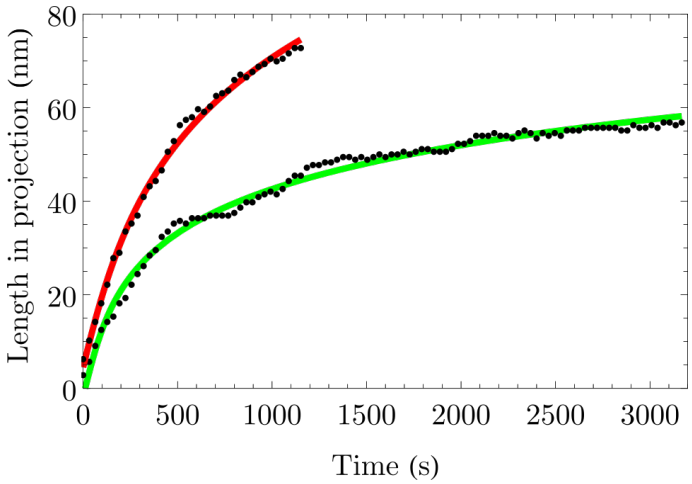

Figure 4.16: Measured and fitted evolution of lengths in time at 500 °C. The function used for fitting: $L = c_1 \cdot \operatorname{arcsinh}(c_2 t + c_3)$. The longest measurement (green curve) is perfectly copied by the function which strengthens the validity of the model.

It would be useful to extract the rate dependence on wire's diameter but as we can see in Fig. 4.18, even when we compare data for wires within one experiment which have the same diameter (here 7 nm), they differ significantly. At least they are all fitted quite well by function $L = c_1 \cdot \operatorname{arcsinh}(c_2 t + c_3)$ which strengthens the hypothesis about the vapour–solid mechanism. The confidence level for every nonlinear fit is 95 %.

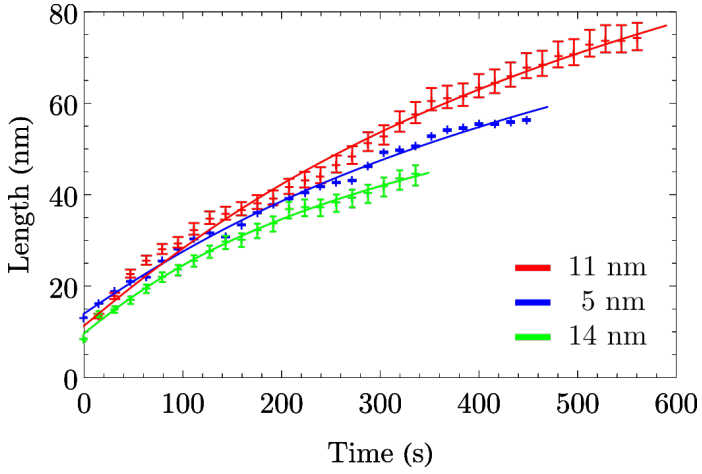

Figure 4.17: Fitted $L(t)$ for three different diameters, 11, 5 and 14 nm ($T = 470\,^{\circ}\mathrm{C}$). Fitting parameters recalculated to have a direct physical meaning are in Table 4.1.

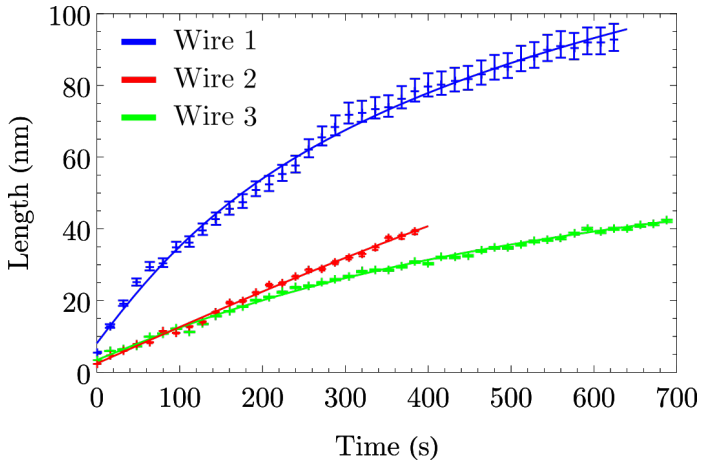

Figure 4.18: Fitted $L(t)$ for three wires which have 7 nm diameter ($T = 470\,^{\circ}\mathrm{C}$). Fitting parameters with error estimates are recalculated to have a physical meaning an are in Table 4.1.

Table 4.1: Diffusion length λ and $V_0 q$ calculated from fitted measured data for real lengths from Fig. 4.17 and 4.18. $V_0 q$ represents the lower boundary condition, i.e. the flux of molecules coming from the nanotube.

Diameter (nm)	λ (nm)	$V_0 q$ (nm^2/s)
5	37 ± 3	0.20 ± 0.03
7	41.6 ± 1.5	0.55 ± 0.05
7	66 ± 19	0.18 ± 0.08
7	23.1 ± 0.8	0.17 ± 0.01
9	70 ± 30	0.19 ± 0.11
11	45 ± 4	0.52 ± 0.09
12	13.6 ± 1.3	0.8 ± 0.3
14	23.5 ± 1.5	0.68 ± 0.10

4.3. Growth Rates for Various Experimental Conditions

Since we already determined how the nanowire without a nanoparticle at its base elongates in time when the conditions are constant (section 4.2), it is possible to change some of them during observation and draw conclusions about their influence. The only problem is that it is always necessary to compare rates within individual nanowires since fine changes on the nanotube as well as geometrical factors have a big impact on the reaction kinetics. On the other hand, we saw that the growth rate changes slowly as the nanowire elongates and so it is usually possible to fit first part of measured $L(t)$ linearly and the error will be acceptable. This approach was used when characterizing the influence of temperature changes. In all experiments apart from those investigating the influence of water pressure, the pressure is in the range (5–10) Pa.

4.3.1. Influence of the Electron Beam

Irradiation by electron beam is known to cause damage to samples (as described in section 2.2) especially for higher accelerating voltages. In these experiments, 12 kV accelerating voltage is used, so knock-on damage is not expected (minimum voltage for S displacement in nanostructured WS_2 for static lattice is 95 kV in [16] or 93 kV based on [49]). Radiolysis, however, could play an important role as its probability increases with higher temperatures.

When one part of the same nanotube is not irradiated while the second one is, and the two are compared, there is a distinct difference between them (Fig. 4.19). At lower temperatures, irradiated part is decorated with nanowires whereas the other only with nanoparticles. If the temperature increases, the difference is in the amount of nanowires which is substantially higher for irradiated regions and they are usually longer as well, unless the number of nanowires close to each other limits the amount of precursor molecules per nanowire. Furthermore, if a nanotube is locally irradiated at elevated temperature with water vapour present and then the beam no longer scans over it, the nanowires are mostly formed in the exposed segments. In vacuum, the combination of annealing and irradiation does not result in changes of XPS spectra which suggests that permanent sulphur vacancies are not formed without the presence of water. The electron beam most likely induces breaking of W–S bonds which would not last without the presence of water because it is attacked by it before relaxation happens. Or it could be that the beam simply adds energy to the system and therefore makes the reactions faster. Additionally, the molecules of water could be decomposed by the beam which would add to the reactivity.

The most obvious question is whether it is secondary electrons, or high energy primary or backscattered ones. To find an answer, we irradiated the substrate in the vicinity of the nanotube lying on a thin membrane of the MEMS chip. As can be seen in Fig. 4.20, despite the fact that almost no backscattered electrons can be produced in a substrate so thin that STEM imaging is possible (penetration depth for silicon nitride is approximately 900 nm for 12 kV electrons), the reaction started in the nearest parts of the neighbouring nanotube. That suggests the key role of SEs. Additionally, we can observe deposition of tungsten oxide in the irradiated area which suggests that the beam promotes conversion of volatile oxide to crystals. As to how specific dwell times and scan rates influence the formation of nanowires, two types of experiments were conducted. Firstly, only dwell time was changed

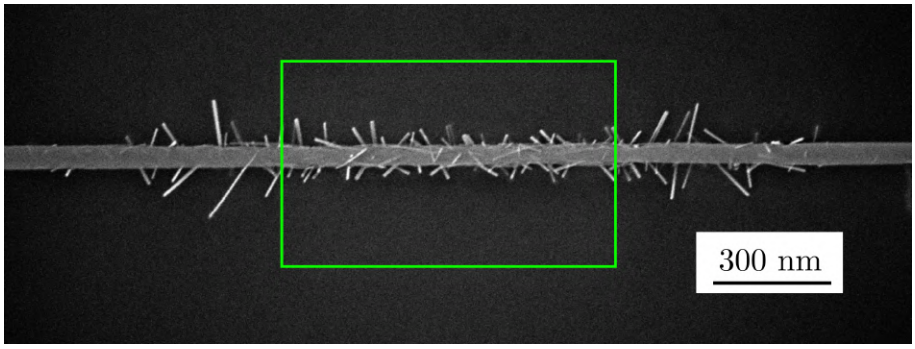

Figure 4.19: A non-uniformly oxidized nanotube which was irradiated in the area marked by the green rectangle. Reaction is started preferentially in the irradiated areas and their vicinity (reaction temperature $T = 500\,^{\circ}\mathrm{C}$).

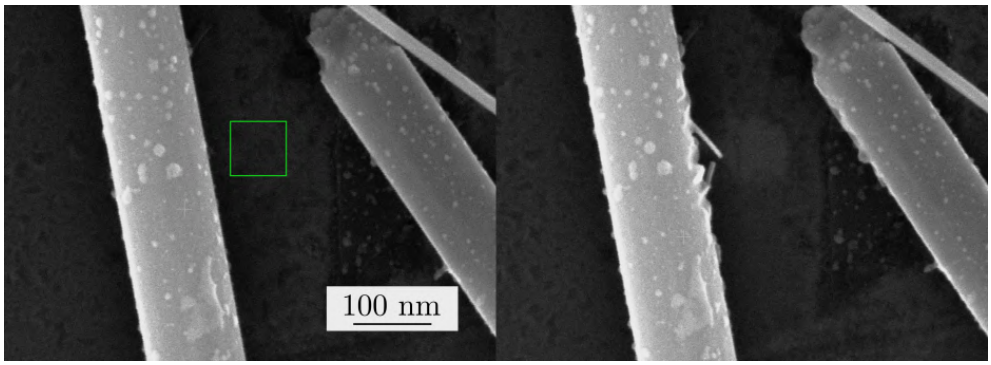

Figure 4.20: Area marked by the green rectangle was continuously irradiated at 530 °C in water vapour for 5 minutes. Some material was clearly deposited as a result of the irradiation and nanowires were formed in the vicinity.

multiple times during an observation of growing nanowire and $L(t)$ was measured. The rates did not change enough to draw the conclusion that some significant radiolytic or heating processes were influencing the growth (see Fig. 4.21). If the beam stays in one place for a longer time, the relaxation is more difficult than for a high scanning rate with low dwell time. In the second type of experiments, times between scans were changed while dwell time was kept at the same value. The rate change was substantial (Fig. 4.22) which suggests that the beam either promotes nucleation of nanowires or increases the flux of tungsten oxide precursor from the substrate. The worst consequence of this finding is the incomparability of experiments with different scanning windows. That is why for example data from Fig. 4.15 and 4.16 (ratio of scanned areas 1:0.7) can not be directly compared to each other and no general assumptions about temperature effects can be made from them.

Based on [30], we know that in TEM, the beam is capable of reducing the nanowires to metallic tungsten. We found out that even at SEM energies, such processes can be observed. Fig. 4.23 shows the splitting of a single nanowire into segments connected by thinned weak points. Because the behavior is very similar to what was reported in [30], the same process is most likely responsible. The reduction takes place both in water vapour and in vacuum.

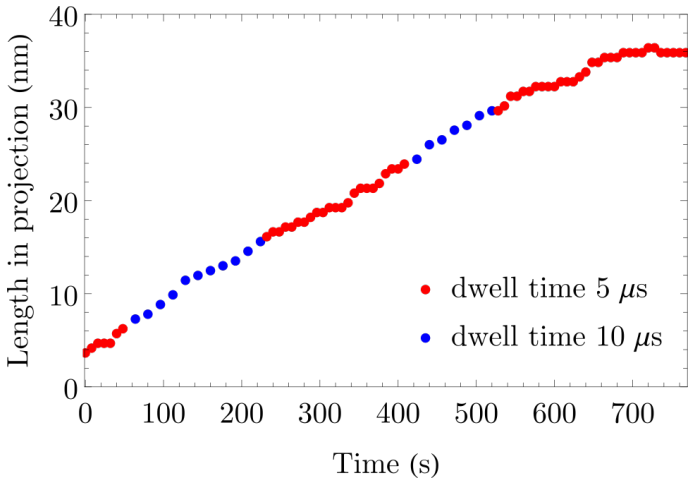

Figure 4.21: Projected length as a function of time for alternating beam dwell times 5 µs and 10 µs. Overall, it is dose rate and not dose which is changed. Temperature was 480 °C. Even if the ratio of dwell times is 1:5, the result is same.

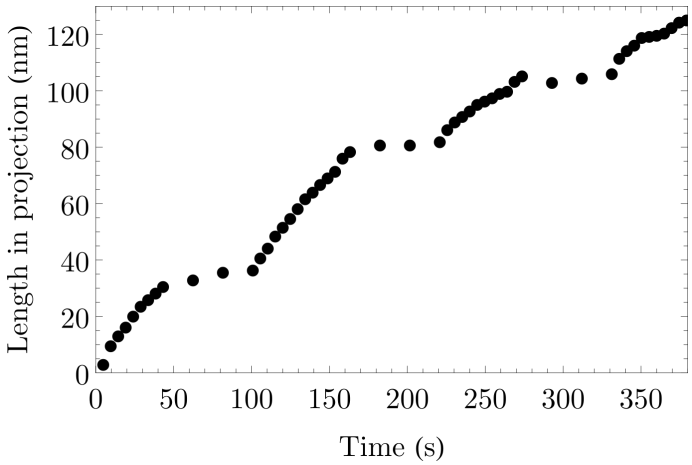

Figure 4.22: Length in projection as a function of time for periodically changing scan frequencies. E-beam clearly enhances the formation of nanowires. Each plotted point corresponds to one scan (frequency 3:1), temperature was 550 °C.

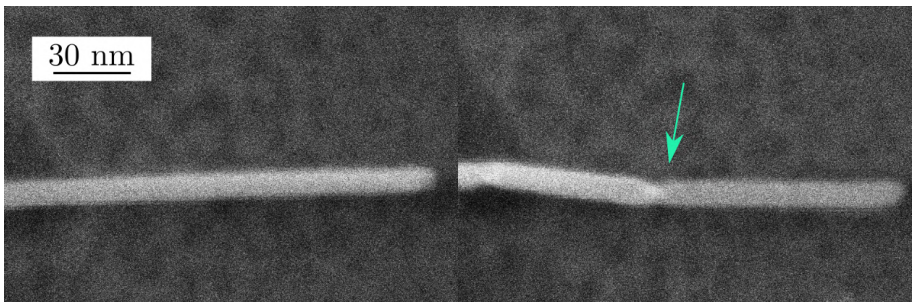

Figure 4.23: At 470 °C in vacuum, a nanowire is significantly damaged by continuous irradiation (12 kV, 100 pA, dwell time 1 µs, dose rate $1.4{\cdot}10^3$ C/(m^{2}s)). A few weak points are created along the wire. Time difference between the two images was 1 minute.

4.3.2. Influence of Temperature

We already have a simplified model

$$L(t) = \lambda \operatorname{arcsinh}\left[\frac{2V_0 q(t+t_0)}{\lambda R}\right],$$

which is in agreement with measured data so far. From that we get

$$\frac{\mathrm{d}L}{\mathrm{d}t} = \frac{2V_0 q}{R\sqrt{1+\left(\frac{2V_0 qt}{\lambda R}\right)^2}}$$

for $t_0 = 0$. This expression is not very transparent so let's look at the limits for low or high t. Low means that term $\frac{2V_0 qt}{\lambda R} \ll 1$ and vice versa. From that we obtain

$$\frac{\mathrm{d}L}{\mathrm{d}t} = \begin{cases} \frac{2V_0 q}{R}, & \text{if } \frac{2V_0 qt}{\lambda R} \ll 1 \\ \frac{\lambda}{t}, & \text{if } \frac{2V_0 qt}{\lambda R} \gg 1. \end{cases}$$

Let's suppose the wire is at the beginning of its growth. We have some idea of the orders of magnitude of the concerned parameters from the measurement in section 4.2 which was done at 470 °C. If we take $\lambda = 50\,\mathrm{nm}$, $V_0 q = 0.2\,\mathrm{nm}^2/\mathrm{s}$, $R = 10\,\mathrm{nm}$, we obtain the condition $t \ll (\gg) 1250\,\mathrm{s}$. If t is half that, then the error in presuming the rate to be constant is 12 %.

Now, we look at the equation with regard to how each term changes with temperature. $\lambda = \sqrt{D_\mathrm{f}\tau_\mathrm{f}}$ changes most drastically since both D_f and τ_f should vary with temperature. We can assume that the flux of molecules from below the wire q changes as well because it is related to the area on the nanotube from which the molecules diffuse towards the wire.

When we put all these ideas together, we conclude that when the wire is short, the most prominent influence on growth rates is due to the flux from below q which is related to the diffusion coefficient on the tube. When the wire elongates further, the dependence is λ/t and we again see that the rate changes proportionally to the change of the diffusion coefficient on the wire. Based on a very simplified examination of the model, if we indeed obtain some form of reasonable Arrhenius plot, the activation energy we will calculate from it can be related to some diffusion process depending on the nanowire's length.

We conducted a few experiments during which temperature was altered such as the one in Fig. 4.24. Fig 4.25 shows examples of Arrhenius plots which were obtained by rapid variation of temperature.

From such plots for six nanowires growing from one nanotube, we could calculate the activation energy as $(1.5 \pm 0.4)\,\mathrm{eV}$ which is a reasonable enough value for diffusion processes. This particular quantitative experiment along with its interpretation can not be regarded as very credible because we neither know exactly what species are involved in the mass transport nor how big error can be expected due the approximation being valid in a small time windows. Moreover, the effects of the beam are engaged as well when observing continuously.

Apart from the impact on reaction kinetics, temperature seems to be the key parameter which decides the average diameter of nanowires. As it increased to about 600 °C in the experiment from Fig. 4.25, the thinnest wires disappear while the thick ones keep growing. Of course, due to widening of the wires over time, it would be difficult to use temperature

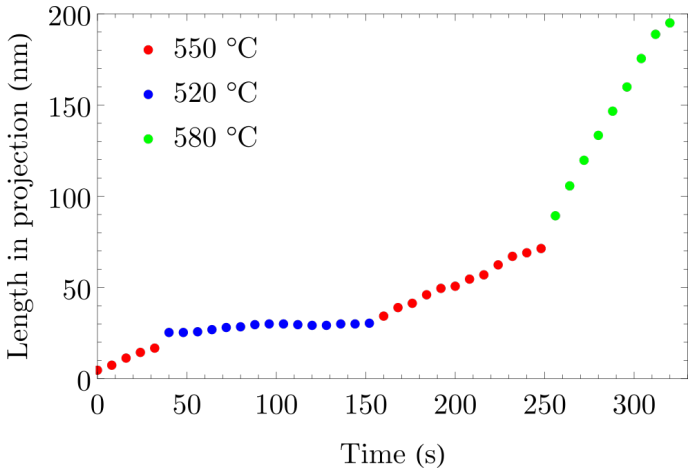

Figure 4.24: $L(t)$ measurement when temperature was changed. In this case, we have a decent amount of data per temperature but only four points for an Arrhenius plot of growth rates were obtained before the rate started to decrease noticeably even for constant temperature.

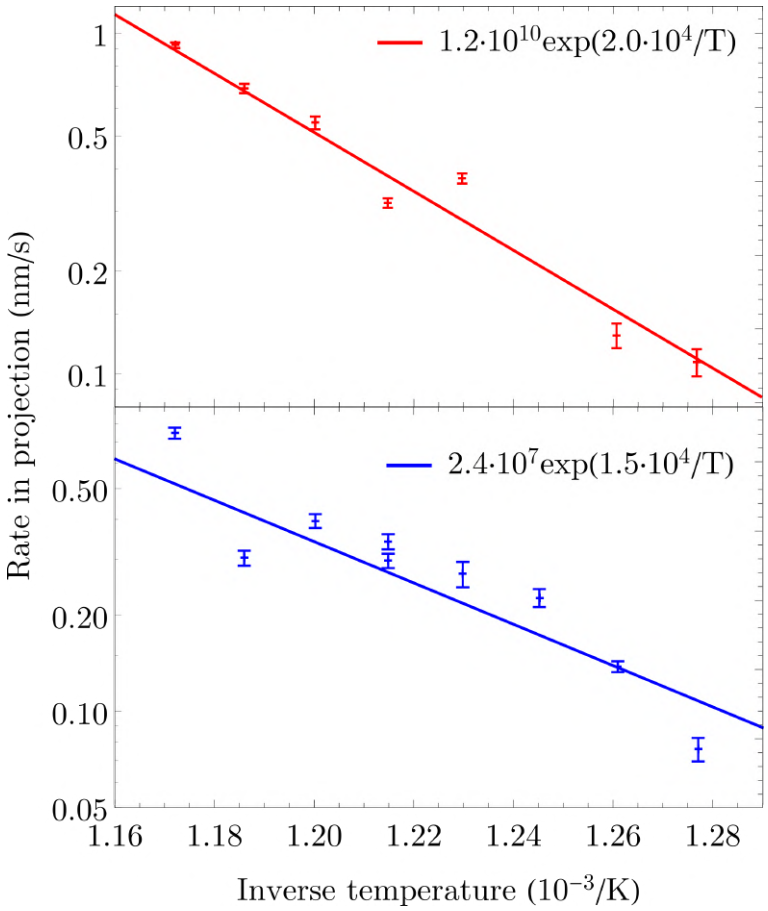

Figure 4.25: Arrhenius plots of growth rates for temperatures in range (510–600) °C. Temperatures were changed after a few scans in random order to avoid biased data and the time in which all the data were collected was approximately 500 s.

as a way to more precisely control their morphology but this effect should be more closely investigated in terms of crystal surface energies and sublimation which is beyond the scope of this thesis.

4.3.3. Influence of Water Vapour Pressure

Since we concluded that the material contributing to the growth is volatile oxide, changing the pressure should change the reaction rate. The amount of water not only determines how fast WS_2 is oxidized, but it should be an important factor for determination of the flux of tungsten oxide vapour molecules on the nanotube and wire. The experiments neither confirmed nor dismissed the hypothesis. It is possible that the range of pressure we can get with our instrumentation is not wide enough to observe significant effects but the growth rate did not change at all even when the pressure was increased from 5 to 20 Pa. The only influence of the pressure we observed, was that for pressures of units of Pa, the initiation of nanowires' growth took very long and started as soon as more water was added. When the wires already nucleated, no change of growth rate was detectable (Fig. 4.26).

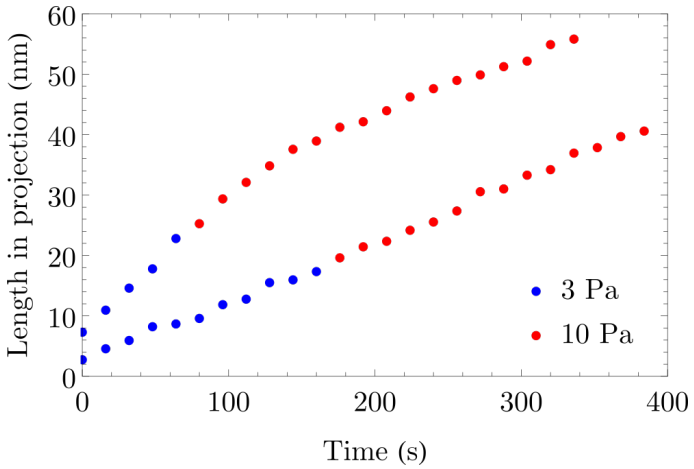

Figure 4.26: Measured projected lengths for wires which were subjected to a rapid change of water pressure from 3 Pa to 10 Pa during growth. Temperature was kept 480 °C during the experiment.

4.4. Cross-Sections of Nanotubes

In light of the fact that the oxide wires mostly emerge from the lower part of the nanotube and not on top, we wanted to verify that the nanotubes have indeed a circular perimeter and their shape is not affected by ultrasonication, interaction with the substrate during solvent drying or by their own weight. If the oxidation affects their inner parts, it would not be well visible in TEM of freestanding nanotubes. We resorted to cross sectioning which was overall not very successful. Since the oxide tends to be milled at different rate than WS_2 unaffected by the reaction, the nanotubes were mostly either too thick for high resolution imaging or collapsed as a result of non-uniform coverage by protective electron beam deposited carbon layer. One of such cross sections is shown in

Fig. 4.27. Interestingly, the nanotubes with oxide particles or wires often had an oxide core as well. Before jumping to a conclusion that the oxidation affects not only the surface but also the core of the nanotubes, comparison with pristine nanotubes was a necessity.

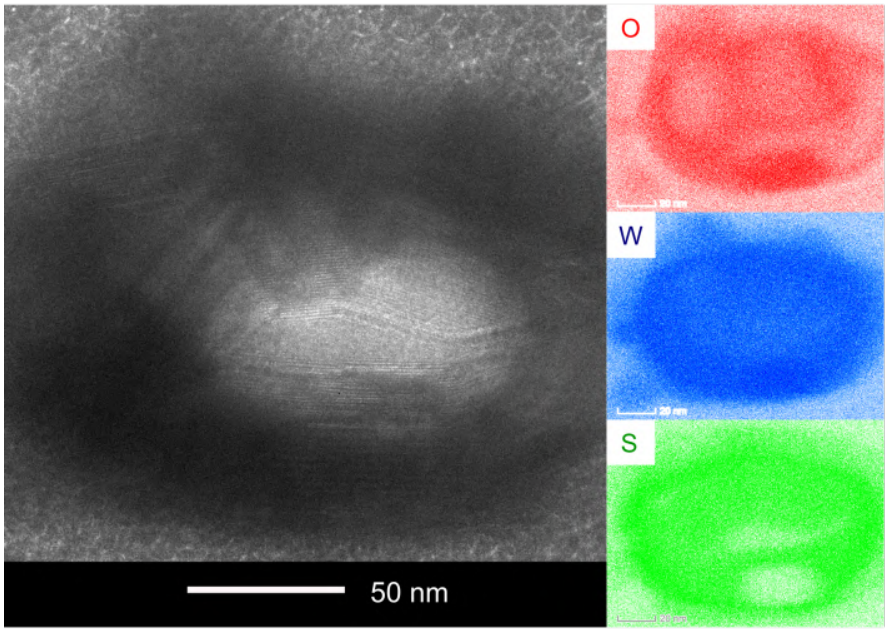

Figure 4.27: Left: Example of a cross-section of an oxidized WS_2 nanotube. The nanotube was not milled uniformly so high resolution imaging or EELS was not possible for all parts of the nanotube and the overall quality of the image is poor. Right: EDS showed that there is oxide not only in the outer layers in the form of particles or wires but oxide structures can be found even within the inner layers.

Cross sectioning of pristine nanotubes revealed that some of them have a hollow core whereas others contain a large amount of oxide (Fig. 4.28). Additionally, especially the hollow ones tend to be significantly distorted when in contact with the substrate or other nanotubes. As a result, it is possible that strain effects promote oxidation at these bent areas. The deformation of cross sectioned nanotubes could be caused by the deposition of protecting layers. However, even if it was done very carefully by a long sequence of alternating depositions from both sides, their shapes were closer to elliptical than circular. Since the nanotubes are used as lubricants, their shape should not be so extensively affected by the process. Only about 2 µm long segment of the tube is covered whereas the rest of it (for example 20 µm) should help maintain the original geometry.

Apart from the well organized outer layers, the more inside of the nanotube we look, the more imperfect the organization of layers gets (Fig. 4.29). This information is not particularly important for the studied reaction but interesting nevertheless.

It is difficult to see any different phase inside the nanotube under standard imaging (nanotube on a TEM grid) and, hence, the cross-sectioning could be capable of revealing much more information. In one of the studied pristine nanotubes, there was no oxygen detectable but the core was filled with tungsten and sulfur in a completely different crystallographic orientations than the outer layers of the tube (Fig. 4.30) and because it is still a layered phase, it seems highly unlikely that it would be a result of redeposition from FIB milling. EDS signal from oxygen was almost equal to noise but Energy filtered

TEM (EFTEM) at energy 532 eV (K edge) proved that oxygen is not present. EFTEM for tungsten (36 eV O edge) nicely shows that the centre has a completely different orientation (Fig. 4.31).

The main conclusion we can draw from the cross sectioning is the following: the nanotubes can look far from ideal and it is very possible that the oxidation process can progress at different rates within the same nanotube due to deformations or local inhomogenities.

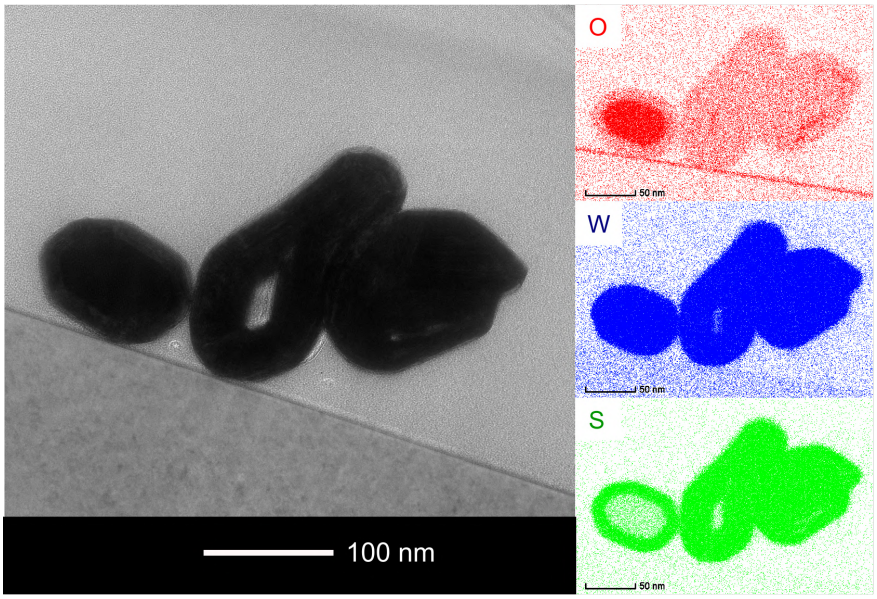

Figure 4.28: Example of a cross-section of pristine WS_2 nanotubes (left). We see two effects very clearly: the nanotubes tend to deform when in contact with each other and they can be in different stages of conversion from oxide to sulfide based on EDS (right).

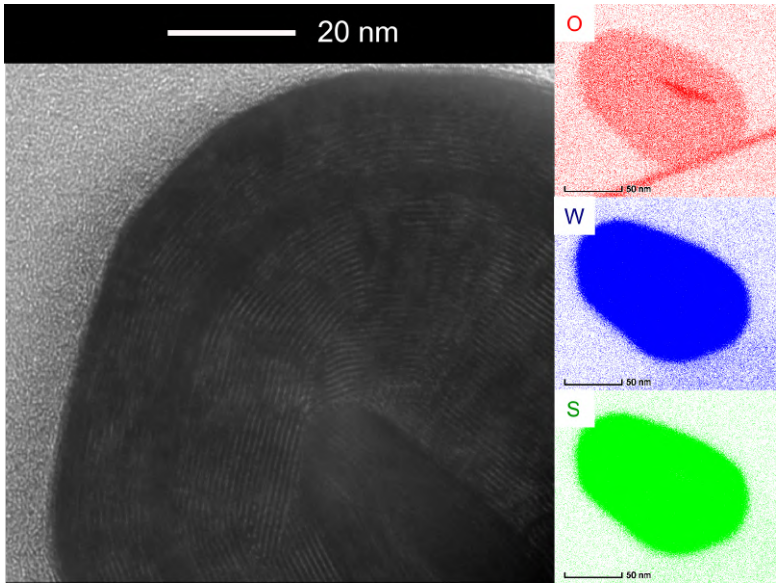

Figure 4.29: Cross section (left) and EDS (right) of a pristine WS_2 nanotube. Only the most outer layers are perfect and there are intermediate layers with different orientations below them. We can also detect a residual oxide core.

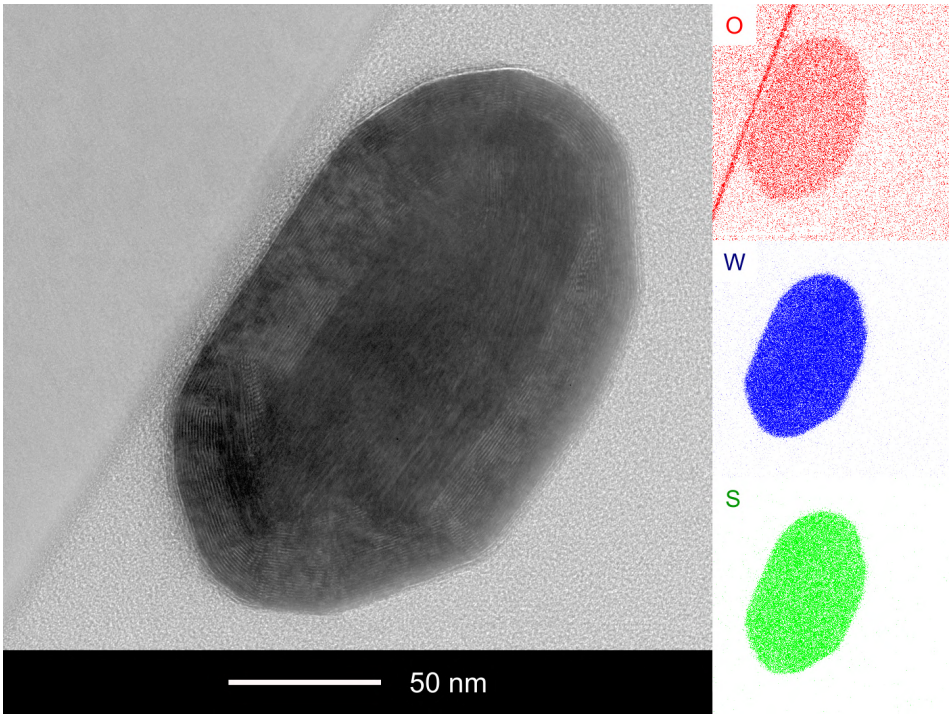

Figure 4.30: Left: TEM image of the cross section of a pristine nanotube which is not hollow. There is no oxide core but the central part has a different crystallographic orientation than the outer layers which is strange. Right: EDS images of the same nanotube proving that the core does not contain oxygen (contrast in the oxygen map was artificially increased for better visibility but the signal is basically just noise).

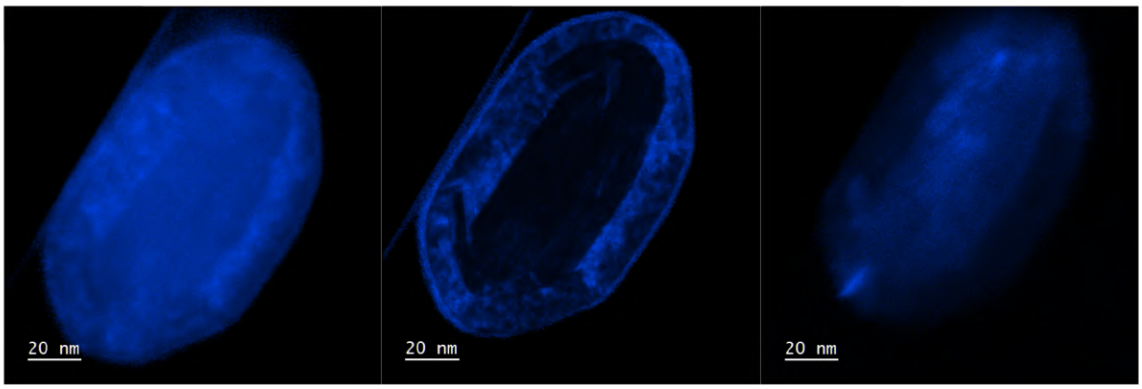

Figure 4.31: EFTEM images at the energy of O edge of tungsten. Left: Signal without the use of objective aperture. The signal is collected from all crystallographic orientations. Middle: Objective aperture inserted. Only the diffraction spot from the outer layers goes through. Right: Objective aperture transmits only the spot corresponding to the core crystal. The measurement was done by Michal Horák.

5. Conclusions

The main aim of this thesis was to study oxidation-reduction reactions in SEM. Oxidation of tungsten disulfide nanotubes and platelets yielding tungsten oxide nanowires has proven to be rather remarkable and complex so it has remained the only subject of this work. Based on the experiments, a simple enough model describing the mechanism of tip growth has been developed and verified by a surprisingly good agreement with the experimental data. By careful analysis of different reaction parameters, we were able to extract how they influence the growth rate.

When exposed to water vapour ($(10^0$–$10^2)$ Pa) at elevated temperatures ((300–450) °C) tungsten disulfide is first decorated with oxide nanoparticles which tend to coalesce along edges of outer sheets by which then possibly reveal the chirality of upper WS_2 layers. After longer annealing, nanowires tend to nucleate from the particles and then rapidly elongate. If the temperature is in the range of (450–650) °C, only few nanoparticles are formed and nanowires mostly grow without particles at their bases.

As was briefly described in 2.4, nanostructured substoichiometric tungsten oxides are a prospective material and methods for their preparation at temperatures lower than 750 °C are in demand. By the described reaction, obtaining nanowires at temperatures below 500 °C with usual diameters (5–20) nm is possible. On the other side, the lengths are usually below 500 nm within hours of reaction and their exact stoichiometry still is an unanswered question.

Based on reports in the literature, we identified that we most likely observe two types of nanowire formation — dominantly by vapour–solid on the tip and by conversion of nanoparticle to a nanowire. The presence of water is crucial as it is known to form volatile compounds with tungsten oxide. The first mechanism has been verified by measurements of evolution of lengths in time when no particles are detected under the wire. Since this process should follow the diffusion equation, a theoretical prediction of the evolution of length in time was built to correspond to our idea about the tip growth when it is not limited by crystallization but rather the flux of volatile molecules towards the growth front. The elongation can be approximated as linear at first and then the rate decreases when the nanowire exceeds the diffusion length and most molecules coming from the base leave the surface before reaching the tip. The growth from nanoparticles is more tricky. Some of the particles completely disappear by transforming into wires but some stay the same as the wire elongates. It suggests that the vapour is is incorporated into the particle as the wire grows similarly to VLS mechanism. Since the wires tend to change their angles they form with the substrate plane during growth when the particle is consumed, it is difficult to capture a reliable $L(t)$ sequence. Another problem is that the root and tip growth are contributing to the elongation at the same time.

Perhaps the most interesting result was the enhancement of the reaction at the sites observed in the SEM. Not only does the beam enable selective oxidation, but its effect on the growth rate is directly observable just by changing the scanning frequency. It most likely enables quicker diffusion of the vapour molecules towards the tip as well as contributes to the substitution of sulfur by oxygen.

Since we established that the process is governed by surface diffusion, changing temperature during the reaction should strongly affect the kinetics. Quickly alternating temperatures and measuring growth rates yielded decent Arrhenius plots and an activation energy of (1.5 ± 0.4) eV was calculated. The energy corresponds to the diffusivity along

WS_2 nanotube since the first part of $L(t)$ plot can be approximated as linearly proportional to the flux of molecules towards the base of the wire.

The only parameter affecting the growth which remains a mystery is pressure of water. Even when increasing water vapour pressure from 5 Pa to 20 Pa, no difference in growth rate was observed. The dependence is most likely very weak in the interval of pressures we can obtain with the instrumentation in SEM.

Obviously, more experiments must be conducted to truly understand the reaction mechanism. One of the most promising methods which could help reveal more about the material transport especially when particles are present, is environmental transmission electron microscopy. We are trying to make that possible through collaboration with other institutions. Identification of the stoichiometry of WO_x nanowires has proven difficult but it is possible that with further analysis of diffraction patterns, we will be able to answer this question. The activation energy obtained by altering temperature during observation of growth should be confirmed by a careful experiment in which there are only two scans per temperature to avoid the combination of e-beam-enhancement and thermal diffusion activation. Because we now have a broader range of pressures (up to 100 Pa) we can work with and still obtain a decent SE signal, the pressure-dependent growth rate will be investigated again.

Bibliography

[1] Flower, H. M. (1973). High voltage electron microscopy of environmental reactions. *Journal Of Microscopy*, *97*(1-2), 171-190. https://doi.org/10.1111/j.1365-2818.1973.tb03772.x

[2] Hashimoto, H., Naiki, T., Eto, T., Fujiwara, K. (1968). High Temperature Gas Reaction Specimen Chamber for an Electron Microscope. *Japanese Journal Of Applied Physics*, *7*(8), 946-952. https://doi.org/10.1143/JJAP.7.946

[3] Takeda, S., Yoshida, H. (2013). Atomic-resolution environmental TEM for quantitative in-situ microscopy in materials science. *Microscopy*, *62*(1), 193-203. https://doi.org/10.1093/jmicro/dfs096

[4] Podor, R., Ravaux, J., Brau, H. -P. (2012). In Situ Experiments in the Scanning Electron Microscope Chamber. In *Scanning Electron Microscopy*. InTech. https://doi.org/10.5772/36433

[5] Taheri, M. L., Stach, E. A., Arslan, I., Crozier, P. A., Kabius, B. C., LaGrange, T., et al. (2016). Current status and future directions for in situ transmission electron microscopy. *Ultramicroscopy*, *170*, 86-95. https://doi.org/10.1016/j.ultramic.2016.08.007

[6] Zheng, H., Zhu, Y. (2017). Perspectives on in situ electron microscopy. *Ultramicroscopy*, *180*, 188-196. https://doi.org/10.1016/j.ultramic.2017.03.022

[7] Ross, F. M. (2012). In-Situ TEM Studies of Vapor- and Liquid-Phase Crystal Growth. In *In-Situ Electron Microscopy* (pp. 171-189). Weinheim, Germany: Wiley-VCH Verlag GmbH & Co. https://doi.org/10.1002/9783527652167.ch7

[8] Podor, R., Ravaux, J., Brau, H. P. (2012). In Situ Experiments in the Scanning Electron Microscope Chamber. In *Scanning Electron Microscopy*. InTech. https://doi.org/10.5772/36433

[9] Cao, J., Wang, Z. J., Huang, X., Rinaldi, A., Greiner, M., Moldovan, G., et al. (2018). The ESEM as In Situ Platform for the Study of Gas-Solid Interactions. *Microscopy And Microanalysis*, *24*(S1), 344-345. https://doi.org/10.1017/S1431927618002210

[10] Vendelbo, S. B., Kooyman, P. J., Creemer, J. F., Morana, B., Mele, L., Dona, P., et al. (2013). Method for local temperature measurement in a nanoreactor for in situ high-resolution electron microscopy. *Ultramicroscopy*, *133*, 72-79. https://doi.org/10.1016/j.ultramic.2013.04.004

[11] Jiang, N. (2016). Electron beam damage in oxides: a review. *Reports On Progress In Physics*, *79*(1). https://doi.org/10.1088/0034-4885/79/1/016501

[12] Egerton, R. F., Li, P., Malac, M. (2004). Radiation damage in the TEM and SEM. *Micron*, *35*(6), 399-409. https://doi.org/10.1016/j.micron.2004.02.003

[13] Reimer, L. (1993). *Transmission electron microscopy: physics of image formation and microanalysis* (3rd ed). Berlin: Springer.

[14] Meyer, J. C., Eder, F., Kurasch, S., Skakalova, V., Kotakoski, J., Park, H. J., et al. (2012). Accurate Measurement of Electron Beam Induced Displacement Cross Sections for Single-Layer Graphene. *Physical Review Letters*, *108*(19). https://doi.org/10.1103/PhysRevLett.108.196102

[15] Egerton, R. F. (2019). Radiation damage to organic and inorganic specimens in the TEM. *Micron*, *119*, 72-87. https://doi.org/10.1016/j.micron.2019.01.005

[16] Komsa, H. P., Kotakoski, J., Kurasch, S., Lehtinen, O., Kaiser, U., Krasheninnikov, A. V. (2012). Two-Dimensional Transition Metal Dichalcogenides under Electron Irradiation: Defect Production and Doping. *Physical Review Letters*, *109*(3). https://doi.org/10.1103/PhysRevLett.109.035503

[17] Zak, A., Sallacan-Ecker, L., Margolin, A., Feldman, Y., Popovitz-Biro, R., Albu-Yaron, A., et al. (2010). Scaling Up of the WS_2 Nanotubes Synthesis. *Fullerenes, Nanotubes And Carbon Nanostructures*, *19*(1-2), 18-26. https://doi.org/10.1080/1536383X.2010.488594

[18] Terrones, M., Terrones, H., Tenne, R., Rao, C. N. R. (2004). Inorganic nanotubes. *Philosophical Transactions Of The Royal Society Of London. Series A: Mathematical, Physical And Engineering Sciences*, *362*(1823), 2099-2125. https://doi.org/10.1098/rsta.2004.1431

[19] R. Tenne, L. Margulis, M. Genut and G. Hodes. (1992). Polyhedral and cylindrical structures of tungsten disulphide. *Nature*, *360*(6403), 444. https://doi.org/10.1038/360444a0

[20] Duan, X., Wang, C., Pan, A., Yu, R., Duan, X. (2015). Two-dimensional transition metal dichalcogenides as atomically thin semiconductors: opportunities and challenges. *Chemical Society Reviews*, *44*(24), 8859-8876. https://doi.org/10.1039/c5cs00507h

[21] Kim, H.-C., Kim, H., Lee, J.-U., Lee, H.-B., Choi, D.-H., Lee, J. –H., Lee, W. H., Jhang, S.H., Park, B. H., Cheong, H., Lee, S.-W., Chung, H.-J. (2015). Engineering Optical and Electronic Properties of WS_2 by Varying the Number of Layers. *Acs Nano*, *9*(7), 6854-6860. https://doi.org/10.1021/acsnano.5b01727

[22] Zak, A., Feldman, Y., Lyakhovitskaya, V., Leitus, G., Popovitz-Biro, R., Wachtel, E., et al. (2002). Alkali Metal Intercalated Fullerene-Like MS_2 (M = W, Mo) Nanoparticles and Their Properties. *Journal Of The American Chemical Society*, *124*(17), 4747-4758. https://doi.org/10.1021/ja012060q

[23] Hong, S. Y., Popovitz-Biro, R., Tobias, G., Ballesteros, B., Davis, B. G., Green, M. L. H., Tenne, R. (2010). Synthesis and characterization of WS_2 inorganic nanotubes with encapsulated/intercalated CsI. *Nano Research*, *3*(3), 170-173. https://doi.org/10.1007/s12274-010-1018-0

[24] Tenne, R. (2003). Advances in the Synthesis of Inorganic Nanotubes and Fullerene-Like Nanoparticles. *Angewandte Chemie International Edition*, *42*(42), 5124-5132. https://doi.org/10.1002/anie.200301651

[25] Nath, M., Govindaraj, A., Rao, C. N. R. (2001). Simple Synthesis of MoS_2 and WS_2 Nanotubes. *Advanced Materials*, *13*(4), 283-286. https://doi.org/10.1002/1521-4095(200102)13:4¡283::AID-ADMA283¿3.0.CO;2-H

[26] Rong, Y., He, K., Pacios, M., Robertson, A. W., Bhaskaran, H., Warner, J. H. (2015). Controlled Preferential Oxidation of Grain Boundaries in Monolayer Tungsten Disulfide for Direct Optical Imaging. *Acs Nano*, *9*(4), 3695-3703. https://doi.org/10.1021/acsnano.5b00852

[27] Ly, T. H., Chiu, M. H., Li, M. Y., Zhao, J., Perello, D. J., Cichocka, M. O., et al. (2014). Observing Grain Boundaries in CVD-Grown Monolayer Transition Metal Dichalcogenides. *Acs Nano*, *8*(11), 11401-11408. https://doi.org/10.1021/nn504470q

[28] Tilley, R. J. D. (1995). The crystal chemistry of the higher tungsten oxides. *International Journal Of Refractory Metals And Hard Materials*, *13*(1-3), 93-109. https://doi.org/10.1016/0263-4368(95)00004-6

[29] Sarin, V. K. (1975). Morphological changes occurring during reduction of WO_3. *Journal Of Materials Science*, *10*(4), 593-598. https://doi.org/10.1007/BF00566566

[30] Chen, C. L., Mori, H. (2009). In situ TEM observation of the growth and decomposition of monoclinic $W_{18}O_{49}$ nanowires. *Nanotechnology*, *20*(28). https://doi.org/10.1088/0957-4484/20/28/285604

[31] Yang, F., Huang, K., Ni, S., Wang, Q., He, D. (2010). $W_{18}O_{49}$ Nanowires as Ultraviolet Photodetector. *Nanoscale Research Letters*, *5*(2), 416-419. https://doi.org/10.1007/s11671-009-9499-z

[32] Klinke, C., Hannon, J. B., Gignac, L., Reuter, K., Avouris, P. (2005). Tungsten Oxide Nanowire Growth by Chemically Induced Strain. *The Journal Of Physical Chemistry B*, *109*(38), 17787-17790. https://doi.org/10.1021/jp0533224

[33] Hu, W. B., Zhu, Y. Q., Hsu, W. K., Chang, B. H., Terrones, M., Grobert, N., et al. (2000). Generation of hollow crystalline tungsten oxide fibres. *Applied Physics A: Materials Science & Processing*, *70*(2), 231-233. https://doi.org/10.1007/s003390050039

[34] Frey, G. L., Rothschild, A., Sloan, J., Rosentsveig, R., Popovitz-Biro, R., Tenne, R. (2001). Investigations of Nonstoichiometric Tungsten Oxide Nanoparticles. *Journal Of Solid State Chemistry*, *162*(2), 300-314. https://doi.org/10.1006/jssc.2001.931

[35] Margolin, A., Rosentsveig, R., Albu-Yaron, A., Popovitz-Biro, R., Tenne, R. (2004). Study of the growth mechanism of WS_2 nanotubes produced by a fluidized bed reactor. *Journal Of Materials Chemistry*, *14*(4). https://doi.org/10.1039/b310609h

[36] Kafader, J. O., Ray, M., Raghavachari, K., Jarrold, C. C. (2016). Role of weakly bound complexes in temperature-dependence and relative rates of M_xO_y + H_2O (M = Mo, W) reactions. *The Journal Of Chemical Physics*, *144*(7). https://doi.org/10.1063/1.4941829

[37] Na, H., Eun, Y., Kim, M. -O., Choi, J., Kim, J. (2016). Low-Temperature Selective Growth of Tungsten Oxide Nanowires by Controlled Nanoscale Stress Induction. *Scientific Reports*, *5*(1). https://doi.org/10.1038/srep18265

[38] Shi, S., Xue, X., Feng, P., Liu, Y., Zhao, H., Wang, T. (2008). Low-temperature synthesis and electrical transport properties of $W_{18}O_{49}$ nanowires. *Journal Of Crystal Growth*, *310*(2), 462-466. https://doi.org/10.1016/j.jcrysgro.2007.10.038

[39] Kossoy, A. (2018). WS2 nanolog: new insight on ugly duckling. *Journal Of Nanoparticle Research*, *20*(2). https://doi.org/10.1007/s11051-018-4131-8

[40] Dellasega, D., Pietralunga, S. M., Pezzoli, A., Russo, V., Nasi, L., Conti, C., et al. (2015). Tungsten oxide nanowires grown on amorphous-like tungsten films. *Nanotechnology*, *26*(36). https://doi.org/10.1088/0957-4484/26/36/365601

[41] Hong, K., Xie, M., Wu, H. (2006). Tungsten oxide nanowires synthesized by a catalyst-free method at low temperature. *Nanotechnology*, *17*(19), 4830-4833. https://doi.org/10.1088/0957-4484/17/19/008

[42] Kasuya, K., Ooi, T., Kojima, Y., Nakao, M. (2008). Real-Time Observation of Growth of Tungsten Oxide Nanowires with a Scanning Electron Microscope. *Applied Physics Express*, *1*. https://doi.org/10.1143/APEX.1.034005

[43] Zhang, Z., Wang, Y., Li, H., Yuan, W., Zhang, X., Sun, C., Zhang, Z. (2015). Atomic-Scale Observation of Vapor—Solid Nanowire Growth via Oscillatory Mass Transport. *Acs Nano*, *10*(1), 763-769. https://doi.org/10.1021/acsnano.5b05851

[44] Hashimoto, H., Tanaka, K., Yoda, E. (1960). Growth and Evaporation of Tungsten Oxide Crystals. *Journal Of The Physical Society Of Japan*, *15*(6), 1006-1014. https://doi.org/10.1143/JPSJ.15.1006

[45] Cui, H., Lü, Y. Y., Yang, G. W., Chen, Y. M., Wang, C. X. (2015). Step-Flow Kinetics Model for the Vapor—Solid—Solid Si Nanowires Growth. *Nano Letters*, *15*(5), 3640-3645. https://doi.org/10.1021/acs.nanolett.5b01442

[46] Novak, L., Kolibal, M., Wu, M., Wandrol, P., Vystavel, T. (2018). Control and in-situ imaging of heat and gas mediated processes in FIB/SEM system. *Microscopy And Microanalysis*, *24*(S1), 808-809. https://doi.org/10.1017/S1431927618004531

[47] Mele, L., Konings, S., Dona, P., Evertz, F., Mitterbauer, C., Faber, P., et al. (2016). A MEMS-based heating holder for the direct imaging of simultaneous in-situ heating and biasing experiments in scanning/transmission electron microscopes. *Microscopy Research And Technique*, *79*(4), 239-250. https://doi.org/10.1002/jemt.22623

[48] Kolíbal, M., Bukvišová, K., Kachtík, L., Zak, A., Novák, L., Šikola, T. (2019). Formation of Tungsten Oxide Nanowires by Electron-Beam-Enhanced Oxidation of WS_2 Nanotubes and Platelets. *The Journal Of Physical Chemistry C*, *123*(14), 9552-9559. https://doi.org/10.1021/acs.jpcc.9b00592

[49] Wang, Y., Feng, Y., Chen, Y., Mo, F., Qian, G., Yu, D., et al. (2015). Morphological and structural evolution of WS_2 nanosheets irradiated with an electron beam. *Physical Chemistry Chemical Physics*, *17*(4), 2678-2685. https://doi.org/10.1039/C4CP04251D

List of Abbreviations

CS	Crystal shear planes
CVD	Chemical vapour deposition
DIEF	Damage due to induced electric fields
EELS	Electron energy loss spectroscopy
EDS	Energy dispersive X-ray spectroscopy
EFTEM	Enegy filtered transmission electron microscopy
(E)SEM	(Environmental) Scanning electron microscopy
(E)TEM	(Environmental) Transmission electron microscopy
FEBID	Focused electron beam induced deposition
FIBID	Focused ion beam induced deposition
FIB	Focused ion beam
MEMS	Microelectromechanical system
PC	Pentagonal columns
SE	Secondary electron
SNR	Signal to noise ration
STEM	Scanning transmission electron microscopy
TMD or MX_2	Transition metal dichalcogenides
VLS	Vapour–liquid–solid
VSS	Vapour–solid–solid
XPS	X-ray photoelectron spectroscopy